Study of the Solar Nuclear ^{3}He(^{3}He, 2p)^{4}He Reaction by OCEAN

Masataka Komori

December, 2000

Abstract

Precise knowledge of thermonuclear reaction rates is important in understanding of energy generation, neutrino flux and of nuclear synthesis in the sun. Due to the Coulomb barrier in the entrance channel, a reaction cross section drops nearly exponentially with decreasing the reaction energy, thus it becomes increasingly difficult to measure the cross section.

In the present work, the compact high-current and low energy ion accelerator facility (OCEAN) for the study of the thermonuclear ^{3}He(^{3}He,2p)^{4}He reaction have been built and tested. They consist of the ECR ion source NANOGAN^{TM}, a multi beam extraction system, a beam transport system including a dipole magnet and two quadrupole magnets, a windowless gas target system with a differential pumping system, a gas circulation and purification system, a beam calorimeter and a ΔE-E counter telescope.

The astrophysical S-factor for the ^{3}He(^{3}He,2p)^{4}He reaction, derived from the cross section expressed as $\sigma(E) = \frac{S(E)}{E} \exp(-2\pi\eta)$, was measured at E_{cm}=39.3, 41.3, 43.3 and 45.3 keV, respectively. The results of 5.62, 5.47, 5.22 and 5.18 MeV·b are in an agreement with those of the previous work. The statistic error is improved by a factor of 3 compared to the previous work. The systematic error is also evaluated by taking into account the uncertainties of the reaction energy, beam intensity, target density and detection efficiency. The total systematic error is estimated to be 3.8 %, which is improved by a factor of 1.4, compared to the previous measurement.

A feasibility to measure the reaction cross section as low as pico-barn, has been shown. The facility can provide the $^3He^{1+}$ beam with an intensity of 1 mA at the target chamber. For such the beam intensity, the cross section for the ^{3}He(^{3}He,2p)^{4}He reaction in the solar Gamow energy region, e.g., σ=pico-barn at E_{cm}=21 keV, can be measured within the statistic error of 10 %, at a running time of about one month.

Contents

1 Introduction

1.1 Standard solar model

The sun is assumed to be spherical and to have evolved quasi-statically for a period of about 5×10^9 yr. Evolution is manifested by the loss of photons from the surface of the star, which in turn is balanced by the burning of protons into α-particles in the core of the sun. This is called as a so-called p-p chain reaction. The overall reaction can be represented symbolically by the relation

$$4p \rightarrow \alpha + 2e^+ + 2\nu_e + 25 \text{ MeV}. \tag{1}$$

Protons are converted to α-particles, positrons, and neutrons, with a release of about 25 MeV of thermal energy for every four protons burned. Each conversion of four protons to an α-particle is known as a termination of the chain of energy-generating reactions that accomplishes the nuclear fusion. The thermal energy that is supplied by nuclear fusion ultimately emerges from the surface of the sun as sunlight.

Energy is transported in the deep solar interior mainly by photons. The pressure that supports the sun is provided largely by the thermal motions of the electrons and ions.

Some of the principal approximations used in constructing standard solar models [1] deserve special emphasis because of their fundamental roles in the calculations. These approximations have been investigated carefully for possible source of departure from the standard scenario.

1. *Hydrostatic equilibrium.* The sun is assumed to be in hydrostatic equilibrium, that is the radiative and particle pressures of the model exactly balance gravity. Observationally, this is known to be an excellent approximation since a gross departure from hydrostatic equilibrium would cause the sun to collapse (or expand) in a free-fall time of less than an hour.

2. *Energy transport by photons or by convective motions.* In the deep interior, where neutrinos are produced, the energy transport is primarily by photon diffusion; the calculated radiative opacity is crucial ingredient in the construction of a model and has been the subject of a number of recent detailed studies.

3. *Energy generation by nuclear reactions.* The primary energy source for the radiated photons and neutrinos is nuclear fusion, although the small effects of gravitational contraction are also included.

4. *Abundance changes caused solely by nuclear reactions.* The initial solar interior is presumed to have been chemically homogeneous. In regions of the model that are stable to matter convection, changes in the local abundances of individual isotopes occur only by nuclear reactions.

1.1.1 Nuclear fusion reaction

As mention above, the sun shines by converting protons into α-particles. About 600 million tons of hydrogen are burned every second to supply the solar luminosity. The main nuclear burning reactions in the sun are shown in Fig. 1, which represents p-p chain reaction. The fundamental reaction in the solar energy-generating process is the p(p,$e^+\nu$)d reaction. The rate of the p-p chain depends entirely on the rate of the p+p reaction, and the rate of the energy generation depends on how many of the subsequent reactions come into equilibrium with the p+p reaction. The deuteron produced by p+p reaction is burned quickly by a (p,γ) reaction that forms ^{3}He. Below an effective central temperature of T_6=8, which is in units of 10^6 K($\equiv T_6$), the p-p chain terminates at ^{3}He with an energy generation close to one-half that of full chain. In the temperature range about T_6=8$\sim$13, the chain is predominantly by the ^{3}He(^{3}He,2p)^{4}He reaction. At higher central temperatures in stars containing amounts of ^{4}He comparable in mass to hydrogen, completion of the chain will be mainly via ^{3}He(α,γ)^{7}Be reaction.

Most of time, 86 % in the standard solar model, the p-p chain is terminated by two ^{3}He nuclei fusing to form an α-particle plus two protons. About 14 % of the time, a ^{3}He nucleus will capture an already existing α-particle to form ^{7}Be plus a gamma ray. It is the neutrinos formed after this process that are primarily detected in so-called ^{37}Cl experiment. Nearly always, the ^{7}Be nucleus will undergo electron capture, usually absorbing an electron from the continuum of ionized electrons. Most of the predicted capture rate in the ^{37}Cl experiment comes from the rare termination in which ^{7}Be captures a proton to form radioactive ^{8}B. The ^{8}B decays to unstable ^{8}Be, ultimately producing two α-particles, a positron, and a neutrino. Although the reactions involving ^{8}B occur only once in every 5000 terminations of the p-p chain, the total calculated event rates for the ^{37}Cl and Super Kamiokande experiments are dominated by rare mode.

The nuclear fusion rate and effective energy region is easily derived as follows [2]. The reaction rate per particle pair $\langle\sigma v\rangle$ is written as

$$\langle\sigma v\rangle = \int_0^\infty \phi(v) v\sigma(v) dv \ . \tag{2}$$

$\phi(v)$ represents velocity distribution of reaction particles and $\sigma(v)$ represents the

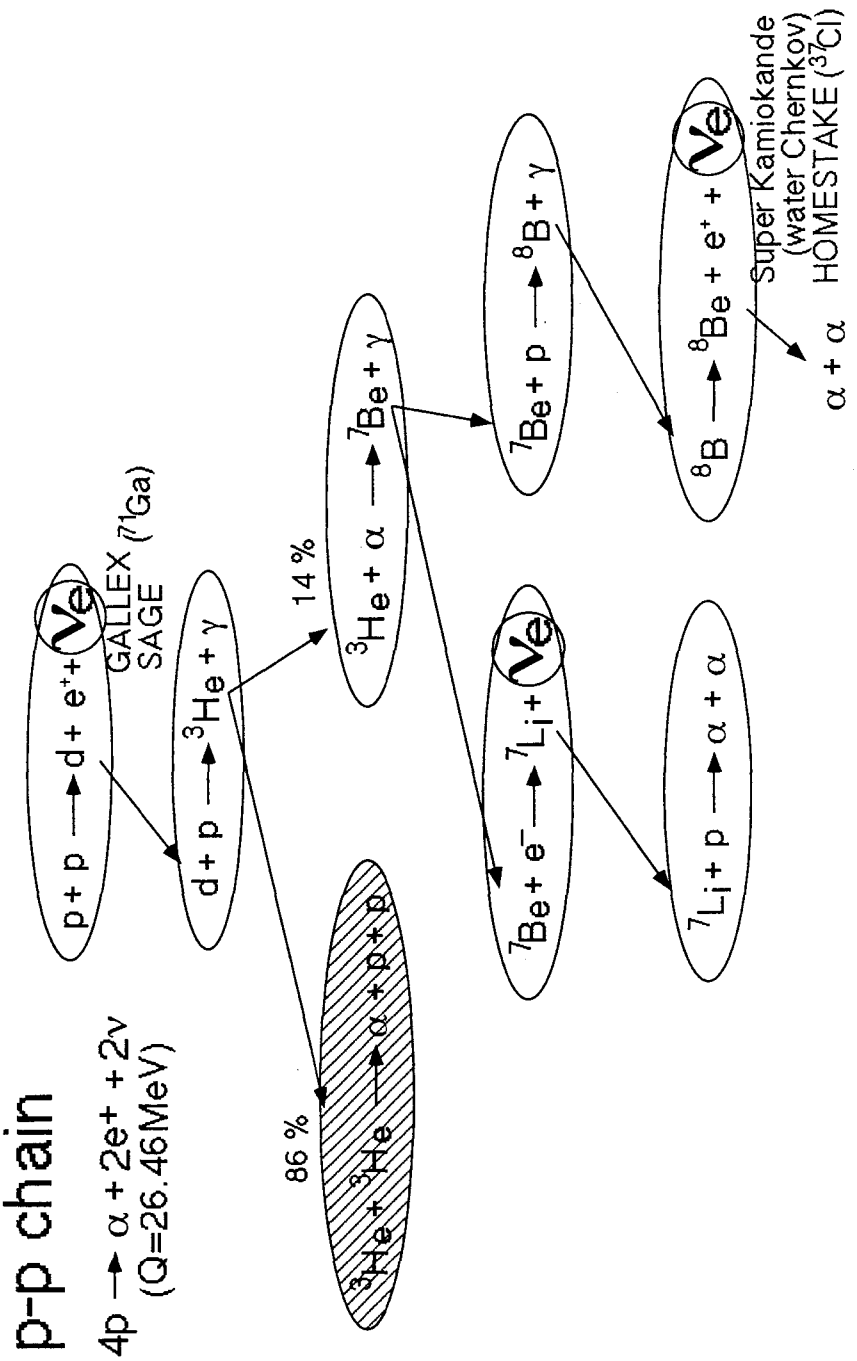

Figure 1: Schematic model of nuclear burning reaction in the sun. The overall reaction can be represented as $4p \rightarrow \alpha + 2e^+ + 2\nu_e + 25$ MeV .

cross section which depends on the reaction energy or, equivalently, the velocity of the reaction particles. In normal stellar matter the gas is in thermodynamic equilibrium, and the velocities of the nuclei can be described by the Maxwell-Boltzmann velocity distribution,

$$\phi(v) = 4\pi v^2 (\frac{\mu}{2\pi kT})^{3/2} \exp(\frac{-\mu v^2}{2\pi kT}) \ . \tag{3}$$

Here T refers to the temperature of the gas and μ to the reduced mass of the interacting particles. If the temperature T is in units of 10^6 K, the numerical value for kT, in keV, is $kT = 0.0862T_6$, and at temperatures in the solar interior the value of kT is 1.3 keV($T_6 = 15$). Inserting formula (3) into (2) and using the center of mass energy $E = \frac{1}{2}\mu v^2$, one obtains,

$$\langle \sigma v \rangle = (\frac{8}{\pi\mu})^{1/2} \frac{1}{(kT)^{3/2}} \int_0^\infty \sigma(E) E \exp(-\frac{E}{kT}) dE \ . \tag{4}$$

Primarily because of the exponential behavior of the probability for tunneling, the cross section for charged-particle-induced nuclear reactions drops rapidly for energies below the Coulomb barrier:

$$\sigma(E) \propto \exp(-2\pi\eta) S(E) \ . \tag{5}$$

Another non-nuclear energy dependent term involves the de Broglie wavelength,

$$\sigma(E) \propto \pi\lambda^2 \propto \frac{1}{E} \ . \tag{6}$$

Using both the equations, one can express the cross section as

$$\sigma(E) = \frac{1}{E} \exp(-2\pi\eta) S(E) \ , \tag{7}$$

where

$$\eta = \frac{Z_1 Z_2 e^2}{\hbar v} \tag{8}$$

is the Sommerfeld parameter and equal to in numerical units $2\pi\eta = 31.29 Z_1 Z_2 (\frac{\mu}{E})^{1/2}$, and the function $S(E)$, defined by this equation and referred to as the astrophysical S-factor, contains all the strictly nuclear effects. Inserting formula (5) into (4) and assuming $S(E) = S(E_0)$=constant, reaction rate is written as

$$\langle \sigma v \rangle = (\frac{8}{\pi\mu})^{1/2} \frac{1}{(kT)^{3/2}} S(E_0) \int_0^\infty \exp(-\frac{E}{kT} - \frac{b}{E^{1/2}}) dE \ , \tag{9}$$

$$b = (2\mu)^{1/2}\pi e^2 Z_1 Z_2/\hbar = 0.989 Z_1 Z_2 \mu^{1/2}(\mathrm{MeV})^{1/2} \ .$$

The penetration through the Coulomb barrier gives rise to the term $\exp(-b/E^{1/2})$, which becomes very small at low energies. The other exponential term, $\exp(-E/kT)$, which vanishes at high energy, is a measure of the number of particles available in the high-energy tail of the Maxwell-Boltzmann distribution. The product of the two terms leads to a peak of the integrand near the energy E_0, which is usually much larger than kT. The peak is referred to as the Gamow peak (Fig. 2). By taking the first derivative of the integrand in equation (6), the energy E_0 for which the integrand has its maximum value, can be found as

$$E_0 = (\frac{bkT}{2})^{2/3} = 1.22(Z_1^2 Z_2^2 \mu T_0^2)^{1/3} \ \ \mathrm{keV} \ . \tag{10}$$

The quantity E_0 is the effective mean energy for thermonuclear fusion reactions at given temperature T. For example, at stellar temperature of $T_6 = 15$, the effective burning energy E_0 for ^{3}He+^{3}He reaction is 21.4 keV.

For the calculations of the reaction rates, precise measurements of the cross sections at effective solar energy region are required. Although, as mentioned above, the reaction cross sections drop nearly exponentially with decreasing the reaction energies, it becomes increasingly difficult to measure the cross sections. Therefore, the rates for solar nuclear reactions are inferred by extrapolating measurements at higher energies to solar reaction energies.

1.1.2 Solar neutrino problem

The solar neutrinos were detected by five experiments, the radiochemical Homestake chlorine experiment [3, 4], the Kamiokande [5] and Super Kamiokande [6] water Cerenkov experiment, and two radiochemical gallium experiments, GALLEX[7] and SAGE [8]. Each radiochemical experiment (Homestake, GALLEX and SAGE) measures one number, the total rate at which neutrinos above a fixed energy threshold (which depends on the detector) are detected. The electronic detectors (Kamiokande and Super Kamiokande) has shown that the neutrinos come from the sun, by measuring the recoil directions of the electrons scattered by solar neutrinos. The detectors have also demonstrated that the observed neutrino energies are consistent with the range of energies expected on the basis of the standard solar model.

The five experiments have all observed neutrino fluxes with intensities that are within a factors of a few of those predicted by standard models [9]. Fig. 3 shows almost everything currently known about the solar neutrino problems. The figure compares the measured and the calculated event rate in the five experiments.

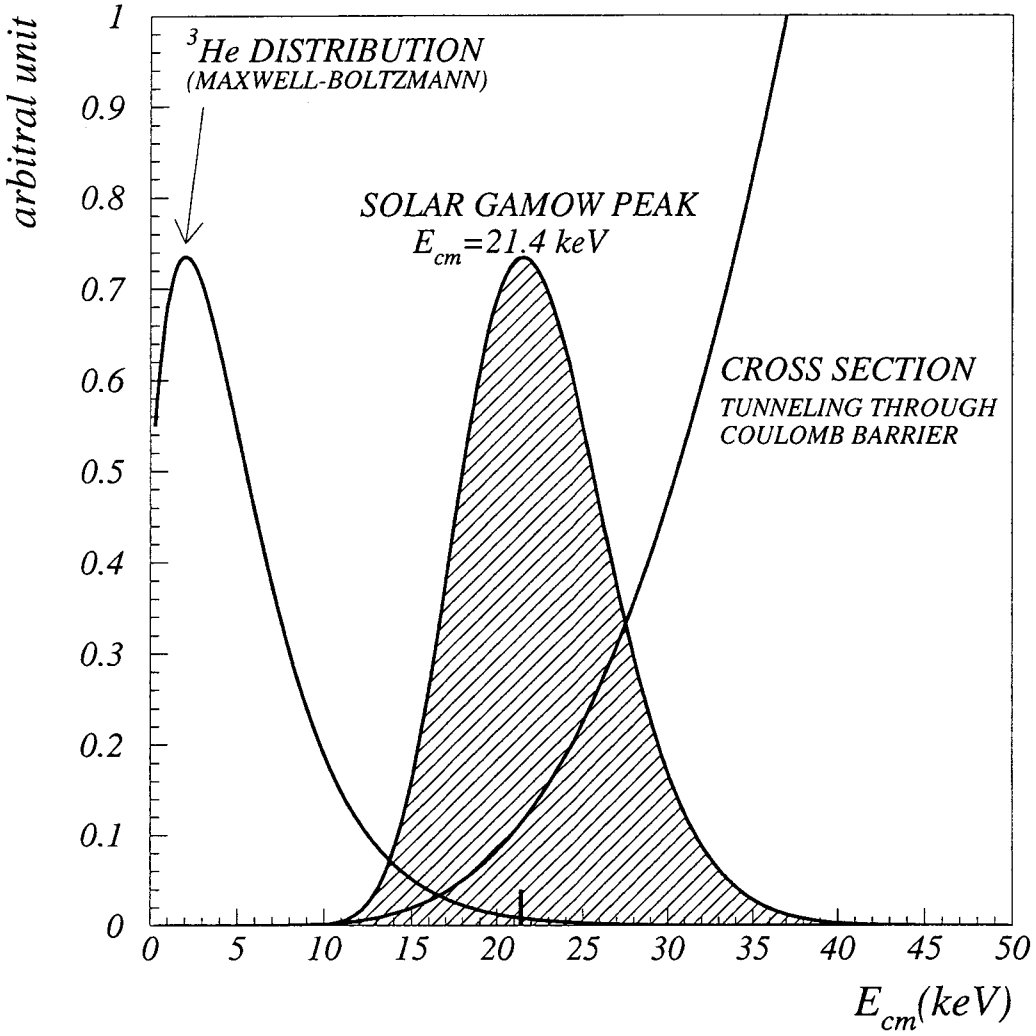

Figure 2: This shows an explanation of the Gamow peak. It is derived from two terms, the tunneling through the coulomb barrier and the high-energy tail of the Maxwell-Boltzmann distribution of interaction particles.

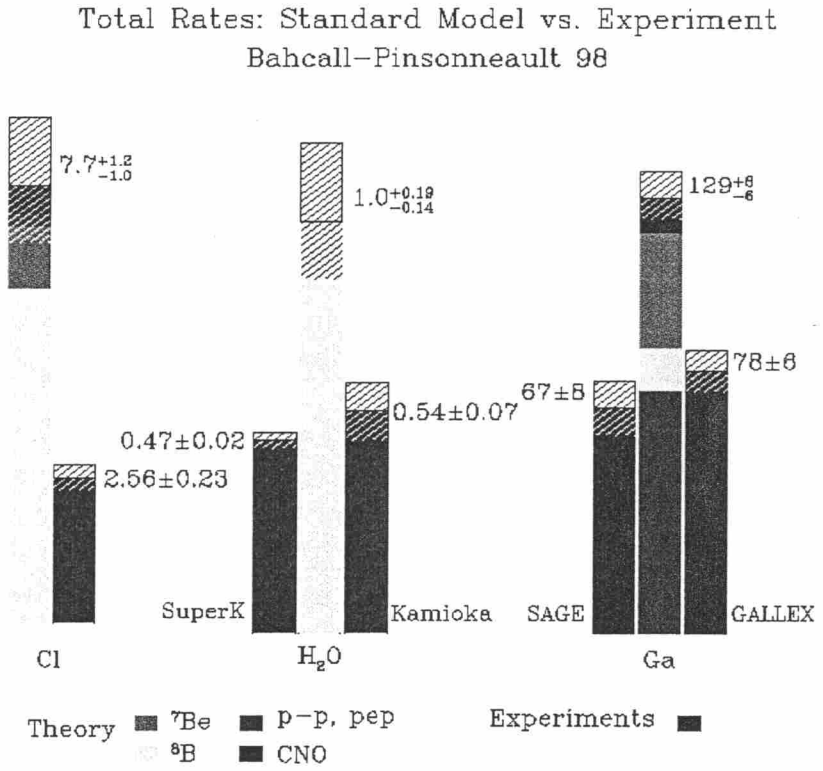

Figure 3: Comparison of measured rates and standard model predictions for five solar neutrino experiments. The GALLEX and SAGE detectors observed the high flux of the low-energy pp-neutrinos, in amount of about two-thirds of the expected flux, while the observed flux of the high-energy neutrinos in (Super) Kamiokande and HOMESTAKE is about a factor 2 and 3 lower than expected, respectively.

The first solar neutrino experiment to be performed was the chlorine radiochemical experiment, which detects electron neutrinos with $^{37}Cl+\nu_e \rightarrow ^{37}Ar+e^-$ reaction which energy threshold is 0.81 MeV. After more than 25 years of the operation of this experiment, the measured event rate is 2.56±0.23 SNU which is a factor ~3 less than is predicted by the theoretical calculations, $7.7^{+1.2}_{-1.0}$ SNU. A SNU is a convenient unit to describe the measured rates of solar neutrino experiments: 10^{-36} interactions per target atom per second. Most of the predicated rate in the chlorine experiment is from the rare, high-energy ^{8}B neutrinos, ^{7}Be neutrinos are also expected to contribute significantly.

The water Cerenkov experiments, Kamiokande and Super Kamiokande, detect higher-energy neutrinos, those with energies above 7 MeV, by the neutrino-electron scattering: $\nu + e \rightarrow \nu + e$. According to the standard solar model, ^{8}B beta decay is the only important source of these higher-energy neutrinos. The measured event rate which is 0.47±0.02 of Super Kamiokande is also a factor ~2 less than the predicted one. Comparing the rates of the Super Kamiokande and the chlorine experiments, it is found that the best-estimated net contribution to the chlorine experiment from the *pep*, ^{7}Be, and CNO neutrino sources is negative, and the contribution to the both experiments from the ^{8}B neutrino source is a factor ~ 2 less than the predicted one.

The results of the gallium experiments, GALLEX and SAGE, constitute the other solar neutrino problem. The average observed rate in these two experiments is 73.4±5.7 SNU, which is fully accounted for in the standard model by the theoretical rate of 72.4 SNU that is calculated to come from the basic *pp* and *pep* neutrinos. The ^{8}B neutrinos, which are observed above 7 MeV in the Super Kamiokande experiment, must also contribute to the gallium event rate. Using the standard shape for the energy spectrum of ^{8}B neutrinos and normalizing to the rate observed in Super Kamiokande, ^{8}B contributes another 6 SNU. Given the measured rates in the gallium experiments, there is no room for the additional 34±4 SNU that is expected [10] from ^{7}Be neutrinos on the basis of standard solar models.

Possible solutions could be found in the fields of neutrino physics, solar physics, or nuclear physics. We discuss here only nuclear aspects: the case of the ^{3}He(^{3}He,2p)^{4}He reaction.

1.2 Uncertainty of the fusion cross section

1.2.1 Electron screening effect

It has generally been believed that the uncertainty in the extrapolated nuclear cross sections is reduced by steadily lowering the energies at which data can be taken in the laboratory. However, this strategy has some complications [11], since

at very low energies the experimentally measured cross section does not represent the bare nucleus cross section. The cross section measured at laboratory is increased by the screening effects arising from the electrons present in the target (and in the projectile). The resulting enhancement of the measured cross section, $\sigma_{\rm exp}(E)$, relative to the cross section for bare nuclei, $\sigma_{\rm bn}(E)$, can be written as

$$f(E) = \frac{\sigma_{\rm exp}(E)}{\sigma_{\rm bn}(E)} \ . \tag{11}$$

Since the electron screening energy, U_e, is much smaller than the scattering energies, E, currently accessible in experiments, one finds [11]

$$f(E) \approx \exp\left\{\pi\eta(E)\frac{U_e}{E}\right\} \ . \tag{12}$$

In the laboratory experiments, the electrons are bound to the nucleus, while in the stellar plasma they occupy (mainly) continuum states. Therefore, the physical processes underlying screening effects are different in the laboratory and in the plasma.

To a good approximation, atomic-target data can be corrected for electron screening effects within the adiabatic limit [12] in which the screening energy, U_e, is simply given by the difference in electronic binding energy of the united atom and the sum of the projectile and target atoms. It appears now as if the electron screening effects for *atomic targets* can be modeled reasonably [13, 14]. This conclusion must be demonstrated for *molecular* and *solid* targets. Experimental work on electron screening with molecular and solid targets is discussed in Engstler *et al.* (1992) [15, 16], while the first theoretical approaches are presented in Shoppa *et al.* (1996) [17] (molecular) and in Boudouma *et al.* (1997) [18] (solid targets).

The enhancement of laboratory cross sections due to electron screening is well established, with the ^{3}He$(d,p)^4$He reaction being the best studied and most convincing example [19, 20]. However, it appeared for some time that the observed enhancement was larger than the one predicted by theory. This discrepancy has recently been removed after improved energy loss data became available for low-energy deuteron projectiles in helium gas [21, 22]. In the recent experiment [23], the enhancement was good consistent with the prediction.

Electron screening effects, estimated in the adiabatic limit, are relatively small in the measured cross sections for most solar reactions. The only major reaction that has so far been studied in the region of the Gamow energy peak is the ^{3}He(^{3}He,2p)^{4}He reaction as will be mentioned in Sec.1.3.2. The data at low energy are enhanced due to electron screening and have been corrected for these effects, however these effects is larger than the adiabatic limit. A more detailed study of

this reaction at low energies is required, with special attention to the region between 15 keV and 60 keV [24].

1.2.2 Hypothetical narrow resonance in the ^{3}He(^{3}He,2p)^{4}He reaction

As early as 1972, there were proposals [25, 26] to solve the solar neutrino problem that suggested a narrow resonance may exist in the ^{3}He(^{3}He,2p)^{4}He reaction at low energies. In 1972, the solar neutrino problem consisted entirely of the discrepancy between the predicted and measured rates in the chlorine experiment [27]. Such a resonance would enhance the ^{3}He +^{3}He rate at the expense of the ^{3}He +^{4}He chain, with important effects for production of the ^{7}Be and ^{8}B neutrinos. For this purpose a resonance with $E_R \simeq 21$ keV and $\Gamma < 6$ keV was considered [28] as the most favorable case. Experimental data available at that time were not inconsistent with the existence of a resonance with E_R=15-20 keV and $\Gamma < 2$ keV [29]. As more data on solar neutrinos became available, it became clear that the deficit of ^{7}Be neutrinos is stronger than that of ^{8}B neutrinos. It was shown [29] that such a pattern of suppression occurs if $E_R < 21$ keV.

Such a resonance level in ^{6}Be has been sought, as will be discussed in Sec.1.3.1, without success by various indirect reaction. In addition, it is not predicted by most nuclear-structure theories. However, the existence of this hypothetical resonance can be positively dismissed only by direct measurements at the required low energies.

1.3 Experimental measurement for the ^{3}He(^{3}He,2p)^{4}He reaction

The solar Gamow energy of the ^{3}He(^{3}He,2p)^{4}He reaction is at $E_0 = 21.4$ keV. As early as 1972, there were proposals [25, 28] to solve the solar neutrino problem that suggested a narrow resonance may exist in this reaction at low energies. Many experiments have been carried out to search for the such narrow resonance by direct measurement of the cross section of the reaction. In addition, indirect measurements that searched for an excited state in ^{6}Be at $E_x \approx 11.6$ MeV that would correspond to a low-energy resonance in ^{3}He + ^{3}He have been carried out.

1.3.1 Indirect measurement

The hypothetical low-energy resonance which would enhance the ^{3}He+^{3}He rate at the expense of the ^{3}He+^{4}He chain, have been investigated by indirect method.

Some experiments have searched for an excited state in ^{6}Be at $E_x \approx 11.6$ MeV that would correspond to a low-energy resonance in ^{3}He+^{3}He reaction(see Table1).

Table 1: Experiments of indirect search for the hypothetical resonance of ^{3}He+^{3}He reaction.

Year	Group	Reaction	ref.
1973	Cardman *et al.*	^{6}Li(p,n)^{6}Be	[33]
1974	Fagg *et al.*	^{6}Li(^{3}He,t)^{6}Be	[34]
1975	Viefers *et al.*	^{4}He(^{3}He,n)^{6}Be	[35]
1977	McDonald *et al.*	^{4}He(^{3}He,n)^{6}Be	[36]

In all attempts no level in ^{6}Be near the ^{3}He+^{3}He threshold has been observed, strongly suggesting that such a level does not contribute to the ^{3}He(^{3}He,2p)^{4}He cross section in the astrophysically interesting energy region. However, all measurements other than direct measurement of the ^{3}He(^{3}He,2p)^{4}He cross section suffer from uncertainties in interpretation [36].

1.3.2 Direct measurement

The energy dependence of the cross section $\sigma(E)$– or equivalently of the astrophysical $S(E)$ factor– for the ^{3}He(^{3}He, $2p$)^{4}He reaction have been observed by various groups as is shown in Table2. The cross sections for the ^{3}He(^{3}He,2p)^{4}He reaction

Table 2: Experiments of direct measurement of the cross section for ^{3}He+^{3}He reaction.

Year	Group	E_{cm} (keV)	ref.
1971	Dwarakanath and Winkler	80 - 1100	[39]
1974	Dwarakanath	30 - 150	[40]
1987	Krauss *et al.*	24.5 - 343	[41]
1998	LUNA Collaboration	20.8-24.8, 45.8-91.7	[42] [43] [44]
1999	LUNA Collaboration	16.5 - 24.4	[45]

have recently been measured at the energies covering the Gamow peak by LUNA experiment. In all of these measurements, a gas target with differential pumping system was used and a beam intensity was measured by a calorimetric method. In the

measurements of Dwarakanath(1971) and LUNA(1998), ΔE-E Si counter telescope was used to identify the protons emitted the reaction and to measure the energies. In the measurements of Krauss(1987) and LUNA(1999), the energies of the protons was measured by Si detector without ΔE-E analysis but $S(E)$ was derived with the proton-proton coincidence analysis. In the measurement of Dwarakanath(1974), the proton-proton coincidence analysis was not carried out, although they did not use ΔE-E counter telescope that meant they could not identify the particle type. Therefore the data has relatively large uncertainties – in comparison to other data sets – and the absolute $S(E)$ values are lower by about 25 %. Then, the data is omitted to calculate the reaction rate of the ^{3}He(^{3}He,2p)^{4}He reaction in standard solar model [24]. The recent experiment of LUNA(1999) measured $S(E)$ at lowest energy region in these experiment. Since the cross section is an order of 0.1 pico-barn at $E_{cm} <$ 20 keV, the data has a large statistical error of 100 %.

Fig. 4 shows the data of Dwarakanath(1971), Krauss(1987) and LUNA(1998). The data provide no evidence for a hypothetical low-energy resonance over the entire energy range that has been investigated experimentally. However, in the energy range between 25 and 50 keV of center of mass energy, the astrophysical S-factor has not been measured precisely by LUNA group. The data of LUNA(1998) was obtained by the 50 kV accelerator and it could only generate singly ionized projectiles, which could not measure the S-factor in such energy range. From the results of Krauss(1987) experiment, the theoretical prediction [29] excluded such energy region for the position of the resonance. Therefore, there are a possibility to find in the energy range 25~50 keV.

In addition, there is a difference of measured S-factor between Krauss(1987) and LUNA(1998). The results of LUNA are much enhanced by the effects of laboratory atomic electron screening [11] than those of Krauss. Because the low-energy ^{3}He(^{3}He,2p)^{4}He measurements must be corrected in order to determine the bare nuclear astrophysical S-factor, it is important to estimate the effect of laboratory atomic electron screening. LUNA(1998) have converted laboratory measurements $S_{\rm lab}(E)$ to bare nuclear S-factor $S(E)$ using the relation

$$S(E) = S_{\rm lab}(E) \exp(-\pi\eta(E)U_e/E) \tag{13}$$

with U_e= 240 eV of the adiabatic limit. The data seem to suggest that the effective value of the electron screening potential may be larger than the adiabatic limit, and the difference is not understood. Therefore, the measurement of the ^{3}He(^{3}He,2p)^{4}He reaction in the energy range between 20 and 50 keV is important to search for the hypothetical resonance and to make a best evaluation of the electron screening effect.

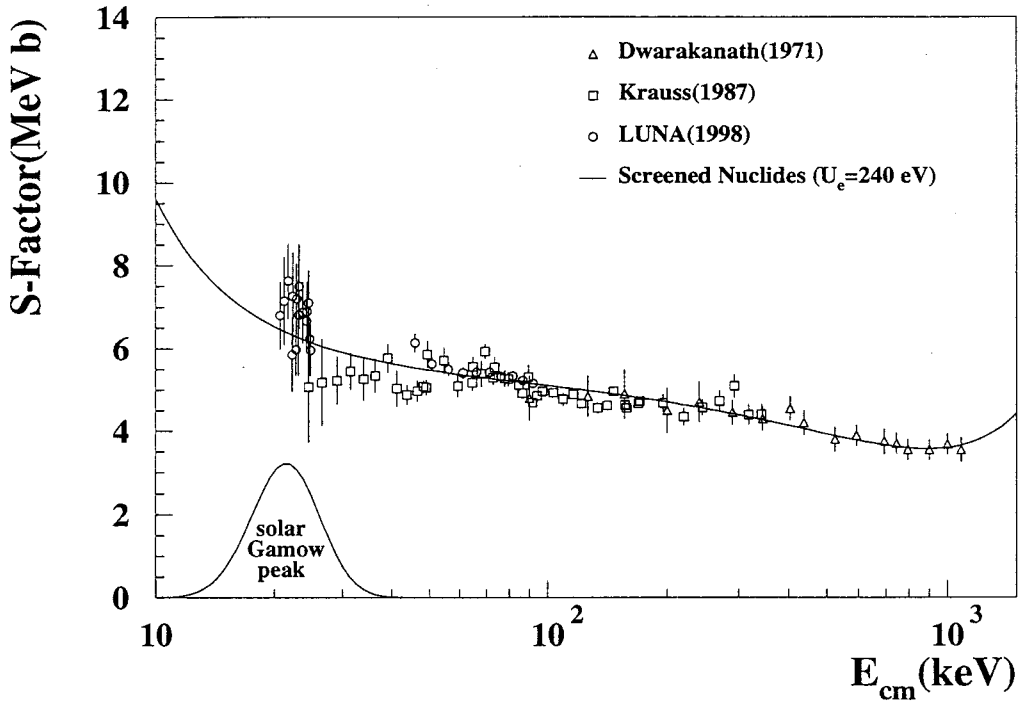

Figure 4: This figure is adapted from Fig. 9 in LUNA(1998) [44]. The measured S-factor for the ^{3}He(^{3}He,2p)^{4}He reaction is shown, and a fit with a screening potential U_e is illustrated. The solar Gamow peak is shown in arbitrary units. The data shown here correspond to a bare nucleus value at zero energy of $S(0) = 5.4$ MeV·b.

1.4 Requirements to the experimental facility

The cross section of the ^{3}He(^{3}He,2p)^{4}He reaction is of the order of pico-barn at the solar Gamow energy region because of the Coulomb barrier. Therefore the experimental facility should satisfy the various requirements. In particular, precise measurement is crucial for the investigation of the existing difference of measured S-factor data between Krauss(1987) and LUNA(1998) (see Fig.4). Also, it should be required to search for the hypothetical resonance explained before. In order to discuss these things, the accuracy of an order of 10 % in the measurements of the ^{3}He(^{3}He,2p)^{4}He reaction cross section is preferable, since the results of LUNA are about 40 % higher than the results of Krauss in the solar Gamow energy region. When the facility will satisfy such condition, it can search for the resonance, because the resonance will enhance the S-factor 10 times as large as the result of LUNA and Krauss, from the theoretical prediction [29].

In a design of the experimental facility, a high intensity beam at low energy is taken into account for selecting an ion source. Since the beam energy is very low, the windowless gas target system should be used for the measurement. In such the target system, it is difficult to increase the target density. In such the high intensity and low energy beam, the beam intensity obtained at a target chamber is reduced due to the known effects of space charge repulsion. In order to minimize such space charge effects [46, 47], the distance between the ion source and the target chamber should be as short as possible. Our aim is to obtain over 1 mA for ^{3}He^{1+} beam at the target chamber. Using the beam intensity of 1 mA, the target density of 10^{17} atom/cm^2 and the detection efficiency of 10 %, the counting rate of the ^{3}He(^{3}He,2p)^{4}He reaction is estimated at 100 counts/month at the cross section of pico-barn.

A systematic error, together with the statistic error, is important to measure the cross section of the ^{3}He(^{3}He,2p)^{4}He reaction. The systematic error which arises from the measurement of the beam intensity, the beam energy, the target density and the estimation of the detection efficiency, is required within 5 %. Particularly, special attention is need for the measurement of the beam energy. An uncertainty of 0.1 % of the beam energy corresponds to that of 1 % of the cross section in the solar Gamow energy region, because the cross section drops steeply at energies far below the Coulomb barrier.

In the measurement of the rare events, the background reduction is also important. For the measurement of the cross section of the ^{3}He(^{3}He,2p)^{4}He reaction, the d(^{3}He,p)^{4}He reaction which arises from the contamination in the target ^{3}He gas and the contamination in the ^{3}He^{1+} beam in the form of the HD$^+$ molecule,

will be the most serious background origin. This is because first, the cross section of the d(^{3}He,p)^{4}He reaction is 10^6 larger than that of the ^{3}He(^{3}He,2p)^{4}He reaction second, the energies of the generated particles of p(14.7 MeV) and α(3.7 MeV) from d(^{3}He,p)^{4}He reaction, are close to those from the ^{3}He(^{3}He,2p)^{4}He reaction; p(0$\sim$10.7 MeV) and α(0$\sim$4.3 MeV). In order to reduce this contribution, of course the deuteron contamination should be reduced as much as possible, the detection system should be designed to be able to efficiently distinguish the ^{3}He(^{3}He,2p)^{4}He events from the d(^{3}He,p)^{4}He events.

2 Experimental Facility

The basic conception of the facility (OCEAN) consisted of a powerful ion source, a beam extraction system, a compact beam transport system with a dipole magnet and two quadrupole magnets, a windowless gas target with a differential pumping system, a gas circulation and purification system, a beam calorimeter, and of a ΔE-E counter telescope[48]. The facility was constructed and placed at RCNP.

2.1 ECR ion source NANOGAN^{TM}

We have chosen the NANOGAN^{TM} 10 GHz electron-cyclotron-resonance (ECR) ion source[49] which was provided by PANTECHNIK(see Fig. 5), from several possible ion sources, such as a duoplasmatron, a duopigatron and different models of ECR ion sources, because it has following advantages:

- it generates $^3He^{1+}$ and $^3He^{2+}$ beams of high intensity,
- it does not require frequent changes of a cathode or filament,
- it is stable for a long-term DC operation,
- it has a simple structure,
- it can be easily mounted on a higher voltage terminal.

Indeed the NANOGAN^{TM} can generate about 40 μA of Ar^{8+} at 20 kV of an extraction voltage with 60 W of a forward RF power and 5 W of a reflected power [50]. Sortais *et al.* reported that 1.7 mA of He^{1+} beam was obtained at 13 kV of the extraction voltage with the NANOGAN^{TM} ECR ion source[51]. From these data we could easily foresee the possibilities of obtaining $^3He^{1+}$ ion beams of more than 1 mA, and $^3He^{2+}$ ion beams of more than 100 μA.

The NANOGAN^{TM} can reduce the most serious origin of the background deuteron contamination which is likely to be introduced into an ion source at the replacement of the filament in case of the duoplasmatron ion source, as is mentioned in Sec. 1.4, because NANOGAN^{TM} does not use the filament. Also, such the no use of the filament is very suitable for a long-term experiment.

Due to a compact and simple structure with a permanent magnet, the NANOGAN^{TM} can easily be mounted on a high voltage terminal. The high voltage terminal of OCEAN facility is electrically isolated by a ceramic insulator at the extraction system and also isolated by a Teflon sheet at a RF waveguide. As a result, a high

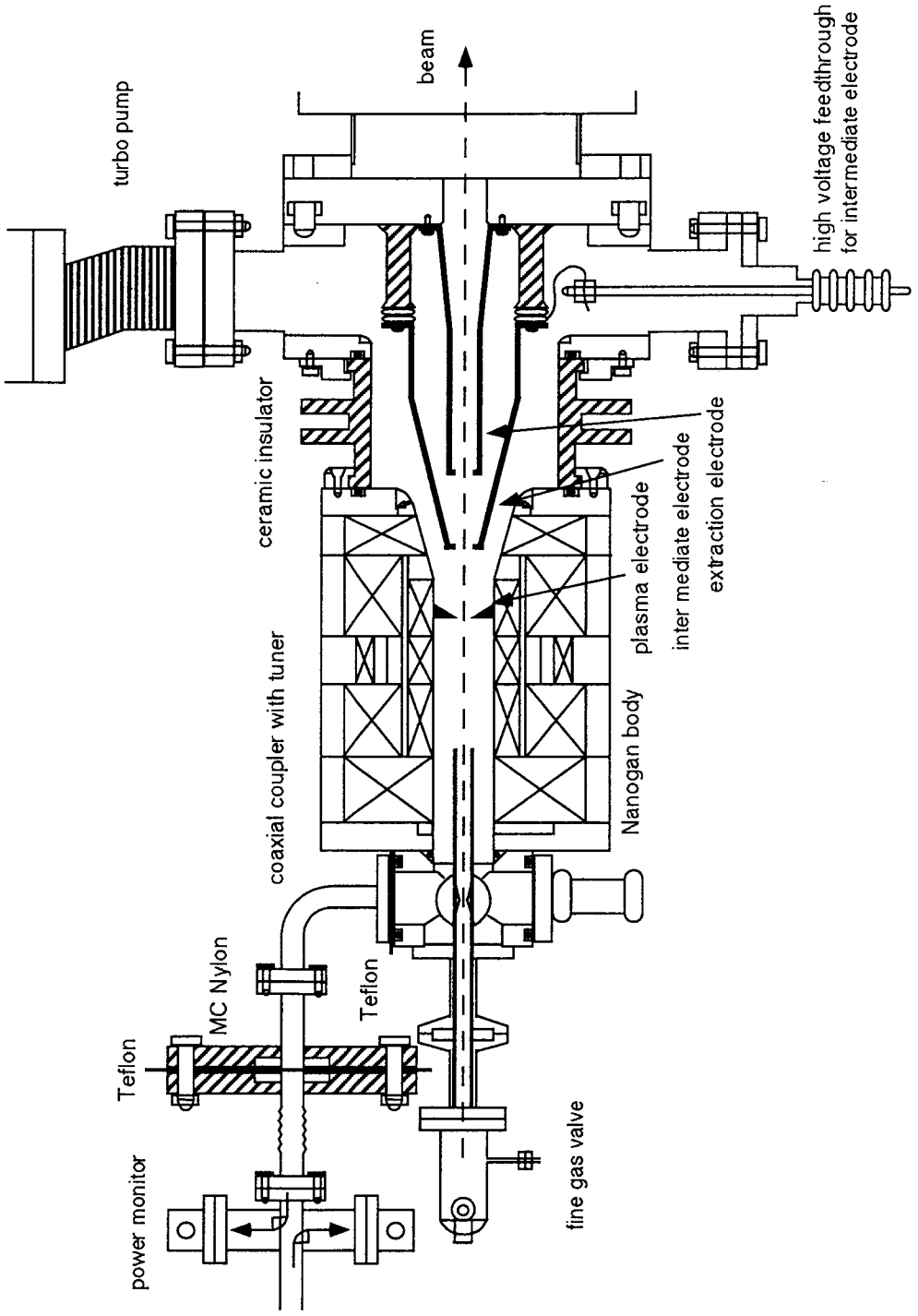

Figure 5: NANOGAN^{TM} ECR ion source and the extraction system of OCEAN facility

voltage up to 50 kV can be supplied to the terminal. The ^{3}He gas is supplied through Teflon tube which also electrically isolates the high voltage terminal and the fine leak valve from a gas cylinder.

2.2 Beam extraction system

2.2.1 Electrode structure

The required energy range of ^{3}He beam is between 50 to 100 keV for $^3He^{2+}$ and between 40 to 50 keV for $^3He^{1+}$ to measure the astrophysical S-factor data for ^{3}He(^{3}He,2p)^{4}He reaction down to solar Gamow peak. In order to apply the extraction voltage up to 50 kV which is 150 % higher than the original NANOGAN^{TM} design, we completely modified the beam extraction system. For this purpose, we designed and tested the multi-electrode extraction system [52, 53]. The multi-electrode extraction system has two advantages as follows:

- It can moderate the electric field gradient originated from the higher extraction potential;
- It can improve the beam emittance even under the condition of a strong ion space charge force.

We have used the computer code FUGUN[54] and optimized the potential, structures, and positions of electrodes to achieve a constant beam emittance and brightness within the expected range of energy changes [55, 56].

The multi-electrode extraction system is shown in Fig. 5. It has three electrodes: the plasma electrode, the intermediate electrode and the extraction electrode. The plasma electrode was installed in the NANOGAN^{TM} body and it stood the extraction voltage up to 50 kV. The intermediate and extraction electrodes were installed in a newly designed cylindrical vacuum chamber. To introduce a high voltage to the intermediate electrode, it was electrically isolated by a ceramic insulator and a high voltage feed-through was placed in the vacuum chamber. From the optimization of the potential by the FUGUN program, the electrode was supplied by about half value of the extraction voltage. The extraction electrode was at the ground potential. Between the NANOGAN^{TM} and the vacuum chamber, a newly designed ceramic insulator was installed. It has a corrugated surface and it has a longer insulation surface length than an original insulator which was too short for applying voltage of more than 20 kV. The vacuum port was added to the chamber to provide direct pumping of the extraction region.

2.2.2 Precise measurement of the acceleration voltage

The high voltage of the ion source was provided by a SL 1200 (SPELLMAN) power supply, with specifications such as max 60 kV/20 mA and stability of 0.02 % per 8 hours. Since the accuracy 1 % of the power supply voltage meter was not sufficient for our study, an external device should be installed in order to measure the acceleration voltage more precisely. We adopted a resistive voltage divider (S-100 provided by Standard Energy Co. Ltd.) with high precision resistor chain of low temperature coefficient, in order to measure the acceleration voltage precisely. The power supply was connected directly to the NANOGAN^{TM} body and the resistive voltage divider. The high voltage was divided with a ratio of 1/10000 by the divider and measured by the digital multi-meter (Model 2000 produced by KEITHLEY Co. Ltd.), with an accuracy of 2×10^{-4}%. The resistive voltage divider was calibrated by the producer in 1997 from 0 to 100 kV range. The result is shown in Fig. 6. It is noted that the divider has a linearity with 0.1 % for the whole range. Therefore, the acceleration voltage was measured with the accuracy of 0.1 %.

2.3 Beam transport system

It is crucial to achieve a high transport efficiency of the beam from an ion source to a target at all over the required energy range. It is also crucial to cope with difficulties by aperture limit of the windowless gas target. By using the multi-electrode extraction system, an invariant beam form could be achieved at the exit of the ion source approximately, despite the fluctuations of the beam. Then the design of the beam transport system is finished successfully to maintain the high transport efficiency and other desirable beam qualities.

At low energy and high beam intensity, the transport efficiency is reduced due to the known effects of space charge repulsion within the ion beam. It is essential to take into account this effect for beam optics to optimize the present beam transport system. Furthermore, the transported beam should be focused at the entrance of the target chamber, since an aperture of the collimator which is installed at such the place, is required to be as small as possible for the differential pumping system. A GIOS computer program by Wollnick *et al.*[57], that incorporates such the space charge effects, was used for the present calculation of our beam transport.

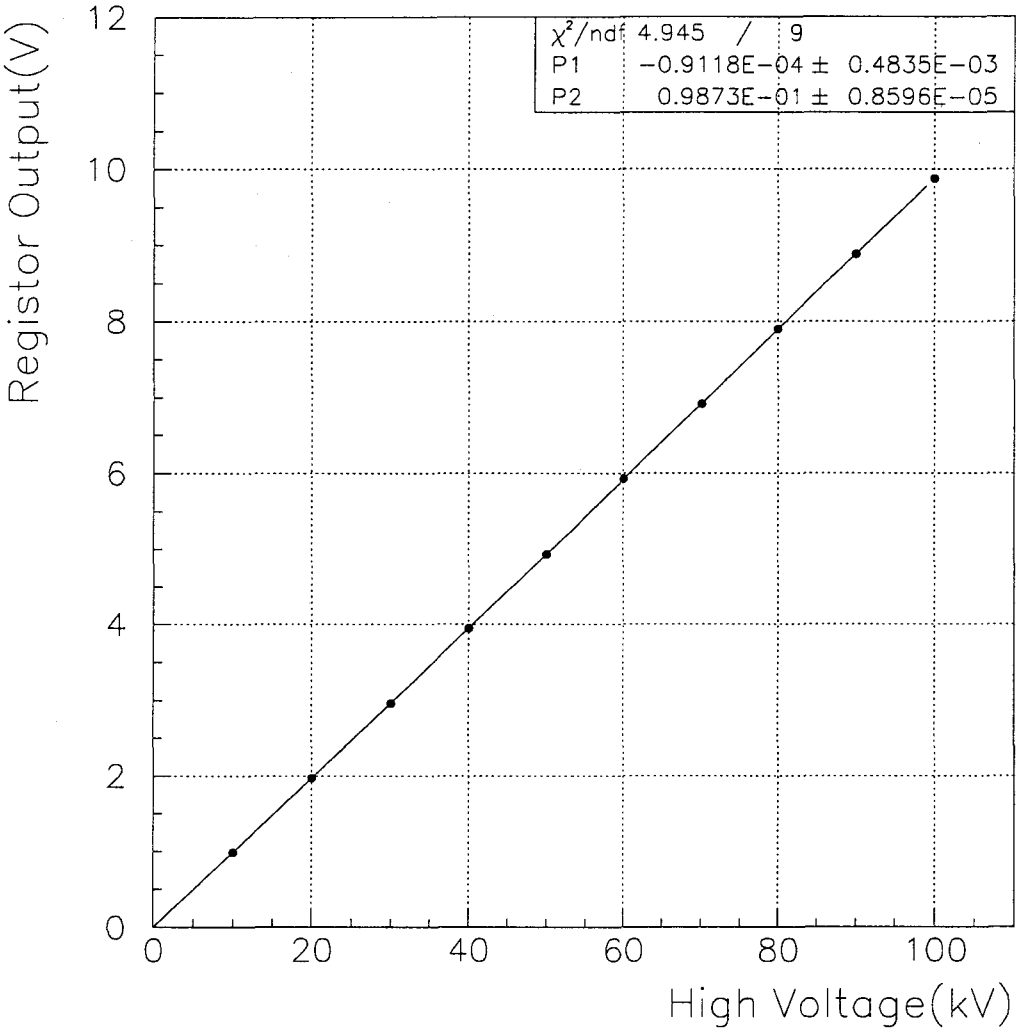

Figure 6: Result of calibration of a resistive voltage divider

2.3.1 Simulation for the beam optics

For the OCEAN facility, we adopted the D(dipole magnet of 90 degree deflection angle)+ Q(quadrupole magnet)+Q transport scheme, because it is easier to operate and it has few elements. To avoid an unacceptable collimator aperture, we calculated the dimension of the beam exactly at the target position varying parameters of the elements and the drift lengths to obtain smaller dx and dy(see Fig. 7). In addition,

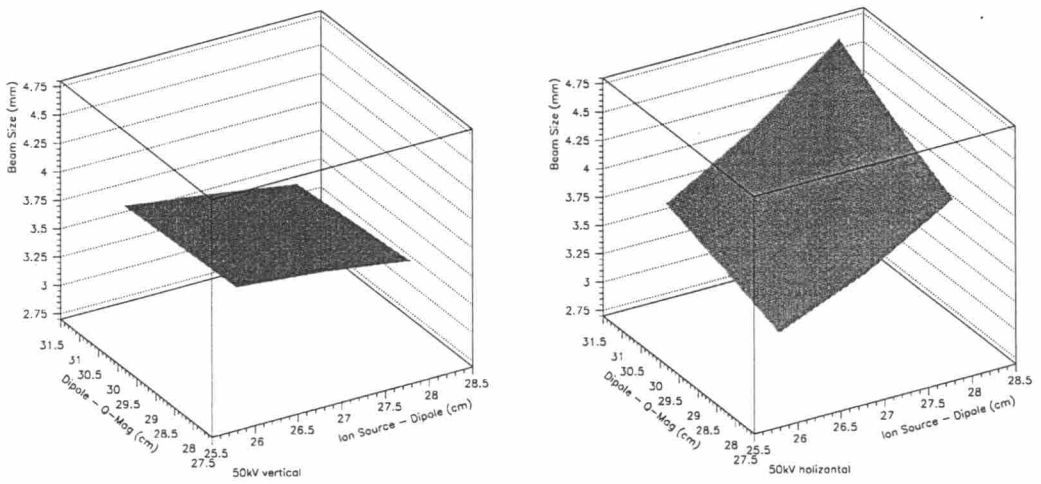

Figure 7: Beam transport calculation for the present designed scheme consisting of the 90° dipole magnet+quadrupole doublet for 1mA 50 keV $^3He^{1+}$ beam. The beam size at the target (vertical and horizontal) was calculated as a function of distance from the ion source to the dipole magnet or from the dipole magnet to the Q-magnet, respectively. The beam source is assumed as 100 πmm mrad emittance.

we considered dx' and dy' to be almost zero, since a strong angular divergence of the beam at the gas target is not suitable for the measurement of a beam intensity using the calorimetric method.

2.3.2 Elements of the beam transport system

The result of the simulation for optimized beam transport system is shown in Fig. 8. In this calculation, we assumed a beam emittance of 100 πmm·mrad. The

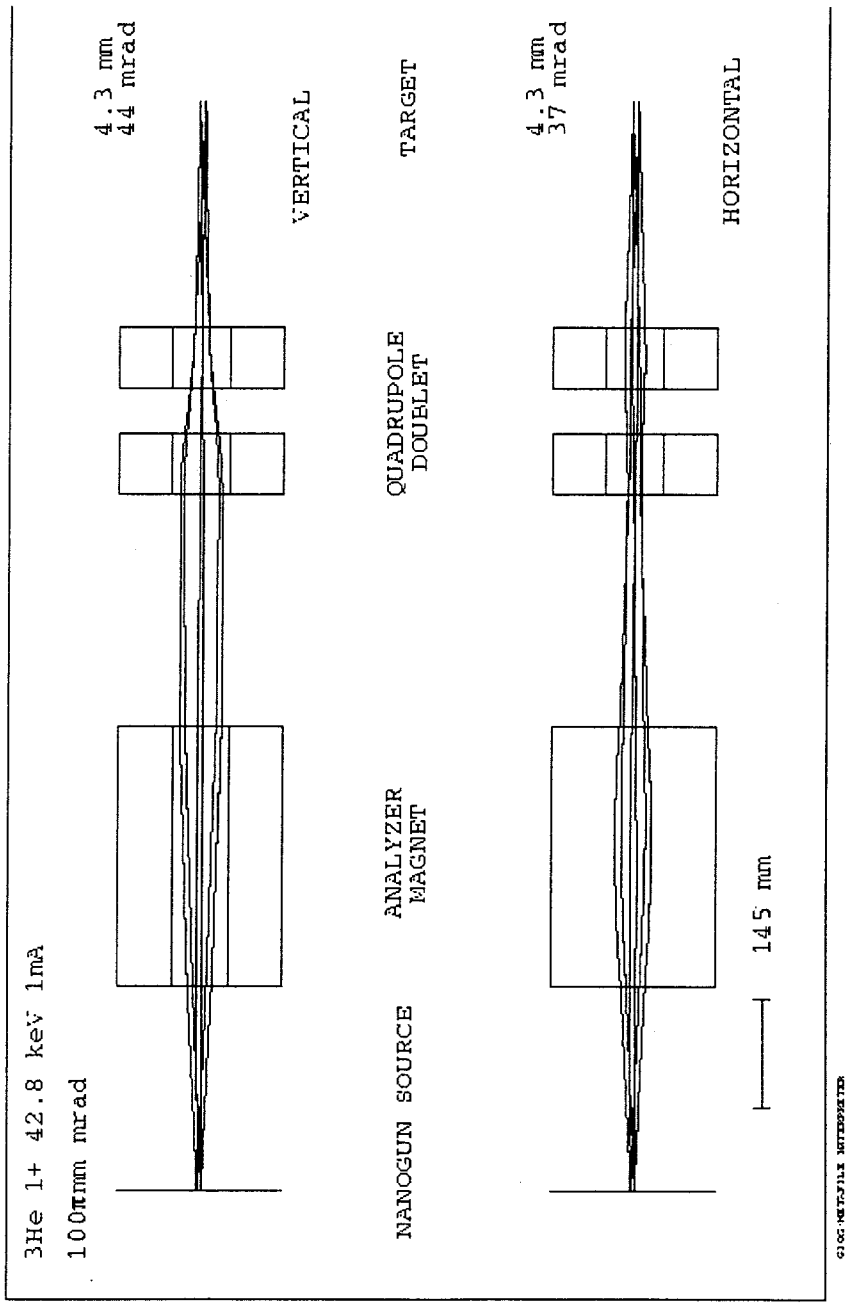

Figure 8: The result of calculation of the beam transport system

distance from the ion source to the dipole magnet is 27 cm which is the closest distance allowed to install several parts such as extraction electrode system, an insulator for applying 50 kV potential and evacuating ports. The specification for the dipole and quadrupole magnets are shown in Table 3,4.

Table 3: Specifications of the dipole magnet

gap	70 mm
pole width	160 mm
central orbit radius	22 cm
entrance and exit angles at pole edge	22°

Table 4: Specifications of the quadrupole magnet

gap	80 mm
length	80 mm

The experimental facility is shown in Fig. 9. This facility consists of the NANOGAN^{TM} ECR ion source, the dipole magnet, two quadrupole magnets, the windowless gas target, the beam calorimeter, and the differential pumping system. The specification of the ion source, the dipole magnet and the Q-magnets are already mentioned. We additionally installed bending magnets for vertical and horizontal beam direction at the entrance and the exit of the dipole magnet, respectively. Also, the beam profile monitor was installed in front of the target chamber to optimize the parameter of the magnets. The total length of the beam path from the ion source to the beam calorimeter is approximately 2 m.

The maximum current of 1200 μA for $^3He^{1+}$ beam and of 130 μA for $^3He^{2+}$ beam were already obtained at the beam acceleration voltage of 40.0 kV. At the same time, the total current of 2.09 mA was measured by the current meter of the high voltage power supply of the beam extraction system. Therefore the beam transmission efficiency was 57 % in this measurement.

2.3.3 Beam mass spectrum

The mass spectrum was obtained by varying a current of the dipole magnet at the applied acceleration voltage of 30.5 kV, as shown in Fig. 10. In the data, the

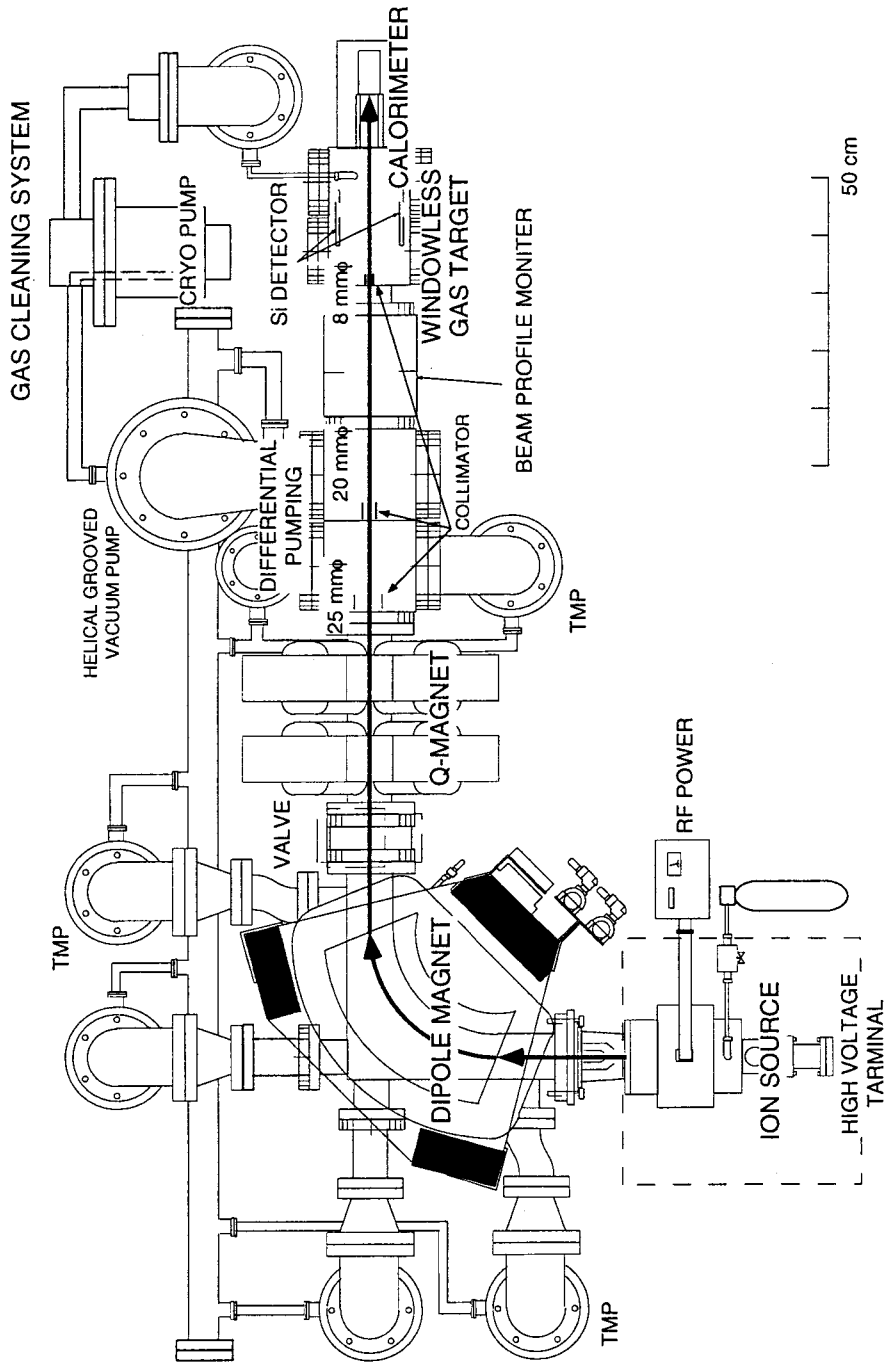

Figure 9: Over view of the experimental facility

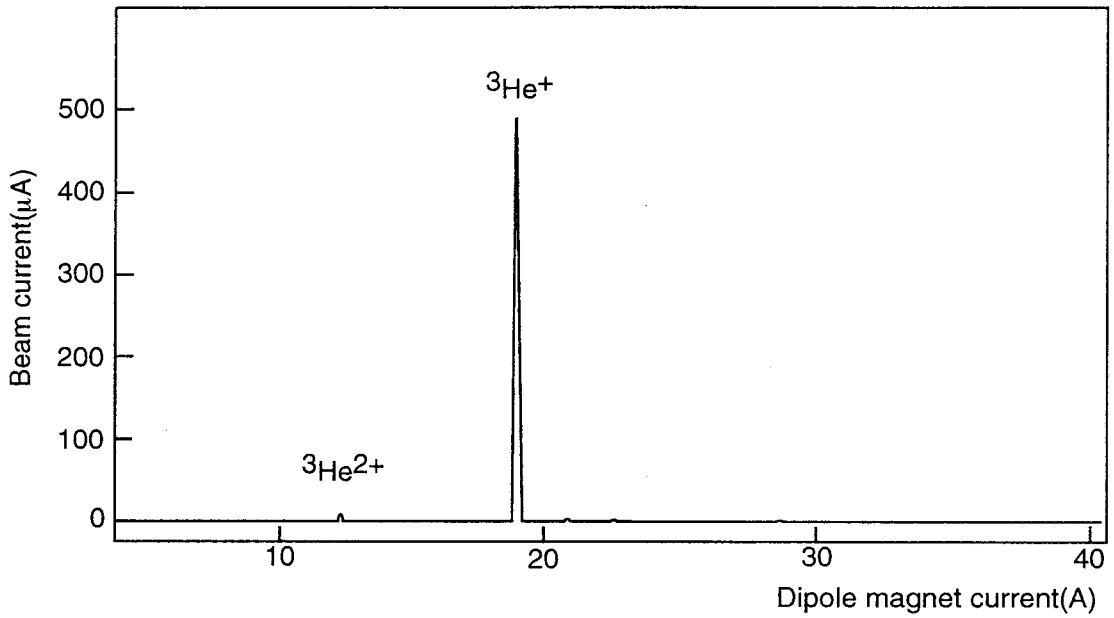

Figure 10: Typical Beam components of the experimental facility

beam current was measured by the beam calorimeter as a Faraday cup as will be mentioned in Sec. 2.5. The Q-magnets were optimized for $^3He^{1+}$ and the dipole magnet current was continuously changed to measure q/m=1 to 1/30.

The mass resolution of the dipole magnet is required to be able to discriminate the deuteron component from the ^{3}He component. As shown in the data, it is found that these components were clearly discriminated, and the deuteron component and a water impurity were scarce. So we could generate very pure ^{3}He beam. However, because of the very small mass difference between HD^{1+} and $^3He^{1+}$, the mass resolution to discriminate them is not compatible with the present high transport efficiency.

2.3.4 Energy resolution

As pointed out in Sec. 2.3.3, the present beam transport system is so based upon the primarily design to get more efficiency than ever achieved in various experimental cites at the lack of the energy resolution. We can estimate the beam energy spread as about a few % taking account of the plasma aperture (objective size of the beam)

and the target collimator and its multiplication factor.

The real energy resolution of this beam transport system was measured. The result is shown in Fig. 11. In this measurement, the dipole magnet and the Q-magnets were optimized to $^3He^{1+}$ beam with extraction voltage of 20.3 kV. The beam current at the target was measured, changing the acceleration voltage from 20.1 to 20.6 kV. The measured energy resolution of the system is about 1%. Energy fluctuations caused by ripples, drifts of high voltage and magnets power supplies are so small that we can determine the beam energy by measuring the potential of the ion source itself during the entire energy range of the beam in this experiment, even if we have to correct the plasma potential for NANOGAN^{TM} ECR source by the reported value of 21.3 $\pm$ 2.4 eV [59].

2.4 Windowless gas target system

The windowless gas target equipped by a differential pumping technique is imperative for the study of ^{3}He(^{3}He,2p)^{4}He reaction, since the energy loss in every window is too large at the beam energy less than 100 keV. The windowless gas target consists of three collimators and various turbo-molecular pumps (TMP). For the expensive ^{3}He gas, the target gas evacuated by the pumping system, was purified and recirculated continuously into the target chamber.

2.4.1 Differential pumping system

For the ^{3}He gas target with the pressure of about 0.1 Torr in the chamber the pumping system should be composed of the three stages between the target chamber and the ion source. The schematic view is shown in Fig. 12. There are three collimators as presented in Table 5 to divide each pumping stage. The specifications

Table 5: Specifications of collimators

	length(mm)	diameter(mm)
collimator A	80	25
collimator B	80	20
collimator C	40	8

are determined mostly by the pumping speed of every stage, as well as by the

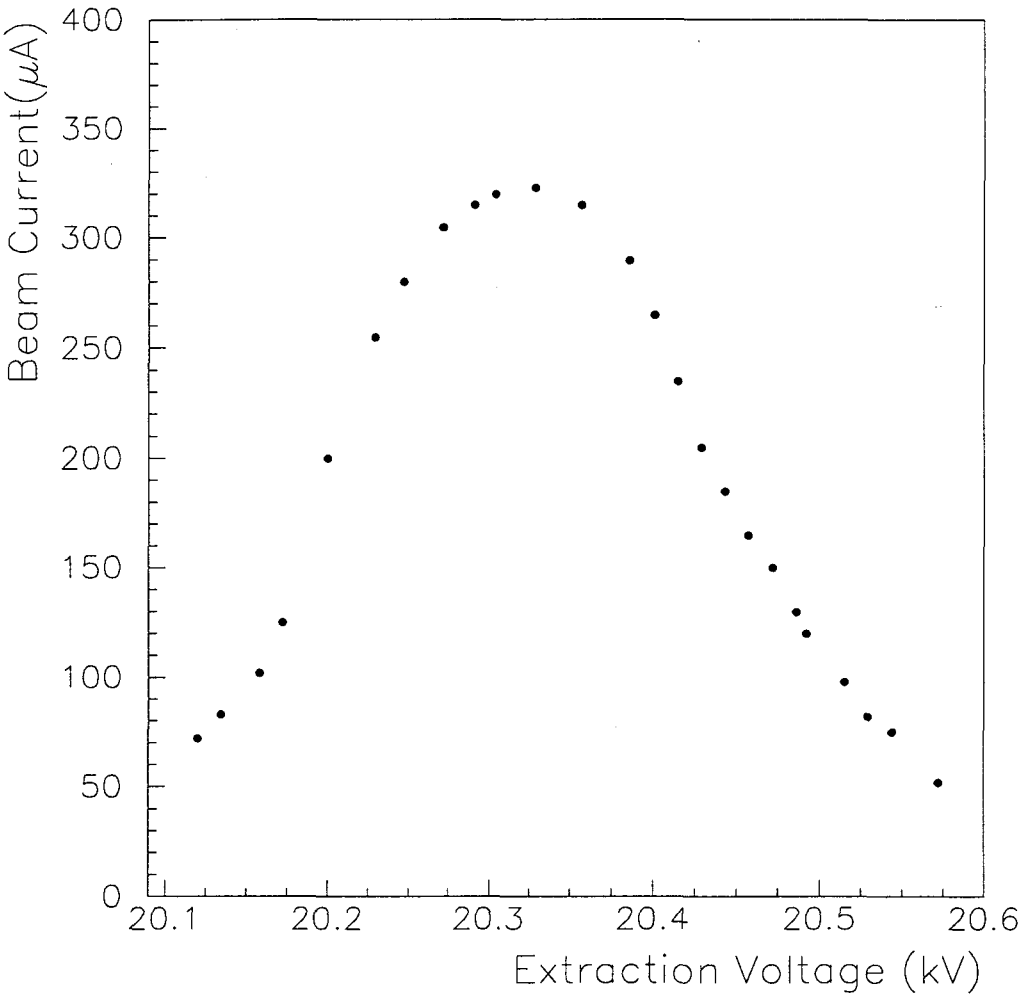

Figure 11: Energy resolution of the beam transport system.

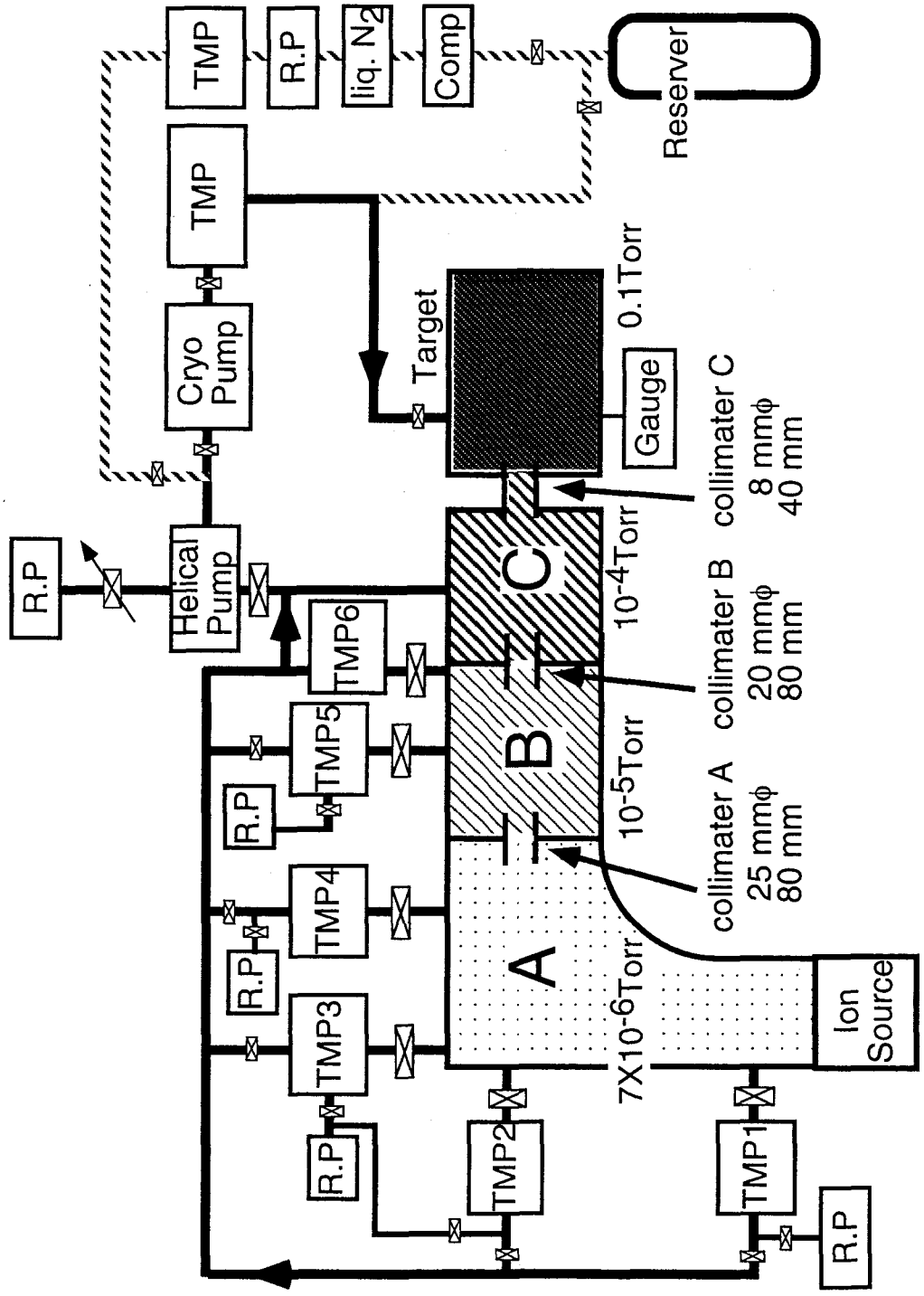

Figure 12: Schematic view of the differential pumping and gas circulation system

estimated conductance of every collimator. In addition, we tested and measured the pressure at various places by applying mechanical booster pumps and several TMP to the test bench modeling a transport system and a target.

We used a helical grooved vacuum pump as a main pump for evacuating the gas flow not only at the viscous region but also at the higher vacuum region. One helical pump was installed for the stage C and other two and four TMPs were installed for stage B and stage A, respectively, (see Fig. 12).

The target gas pressure was measured by a Baratron capacitance manometer (model 127A, MKS) which has an accuracy of 0.16 % at 0.1 Torr. These measurements were absolute and independent of the type of gas used. The gas pressure of other pumping stages were measured by ionization gauges.

The differential pumping system was stable at the target gas pressure from 0.05 to 0.5 Torr. The higher gas pressure seriously affects the pressure increase at the upstream of the beam transport, in particular, at the beam extraction system. The vacuum pressure at the beam extraction system should be as low as possible to avoid a discharge of the beam extraction high voltage. Therefore, the target gas pressure was kept less than 0.1 Torr at our measurements of ^{3}He+^{3}He reaction rates. At the target gas pressure equal to 0.1 Torr, the gas pressures were 1.0×10^{-4} Torr at stage C, 1.0×10^{-5} Torr at stage B, and 7.0×10^{-6} Torr at stage A, as indicated in Fig. 12. The main gas pressure drop occurred due to the collimator C. It was shown that in the extended gas target chamber the pressure in the region for observation by the detectors was essentially unmodified by the gas flow through the collimator C, and the geometrically extended target zone was characterized by a nearly static pressure.

2.4.2 Gas circulation and purification system

For the high quality gas purification and the very expensive ^{3}He gas, the gas from pumping system was purified and recirculated continuously into the target chamber. For the gas purification system, we used a cryo pump which cleaned efficiently the recirculated gas by a trap cooled to liquid helium temperature. In addition, such a purification system is suitable for a long-term measurement, since the cryo pump does not require a frequent maintenance as a liquid nitrogen trap.

The ^{3}He gas from all TMP was recompressed by helical pump, together with the ^{3}He gas from the stage C, and was recirculated into the target chamber through the purification system. The additional TMP was installed between the cryo pump and the target chamber not only to compress the gas into the chamber but also to keep the pressure in the cryo pump low, since the purification efficiency decreases if the

pressure increases. The ^{3}He gas flow increased steadily the gas pressure in the target system for about 20 % per hour at 0.1 Torr region, due to a neutral gas injection into NANOGAN^{TM} ECR ion source, if the differential pumping and gas circulation system was perfectly closed. Therefore the virtual leak was created to compensate such the pressure increase. The total amount of the ^{3}He gas in this system was regulated by separated rotary pumping through a fine leak valve installed after the helical pump.

As mentioned in Sec.1.4, the deuterium contamination in the target gas is a crucial problem for obtaining the cross section data for low energy region. The contamination was estimated as follows. The total system operated in a usual recirculation and purification mode by the cryo pump and TMPs. Without any injection of the target gas, the pressure at the target was maintained at 1.0 $\times 10^{-4}$ Torr. Assuming that the pressure was determined only by a water vapor, the isotopic abundance of deuterium was the same as natural one (0.015 %), and that the deuterium contamination arose due to such the quantity, we can deduce the deuterium contamination (D_2O) as about an order of 0.1 ppm in the presence of ^{3}He gas for the target of 0.1 Torr. This is perfectly low for the study of ^{3}He(^{3}He,2p)^{4}He reaction even in the solar Gamow energy region.

2.5 Beam calorimeter

Under present experimental conditions, such as a low energy beam and a gas target with a pressure of 0.1 Torr, the calorimetric method is only applicable to measure the number of particles. Charge integration with a usual Faraday cup and a commercial current integrator is difficult when a gas target is used, because of charge exchange effects in the ion beam. A novel beam calorimeter was designed and fabricated for OCEAN facility so as to determine the number of incident particles with an accuracy of better than 5%.

2.5.1 Structure of the beam calorimeter and Faraday cup

The structure of the beam calorimeter is shown in Fig. 13. The calorimeter consists of a solid copper heat sink (100mm length, 38mm diameter) with water channels, and a Faraday cup(140 mm, 38 mm diameter, 1.5 mm wall) in front of the heat sink. The Faraday cup is supported by Pyrex glass insulator as well as the metal flange with the Teflon gasket. This organic gasket served not only as a vacuum seal, but also as an electric and heat insulator. Therefore, this calorimeter

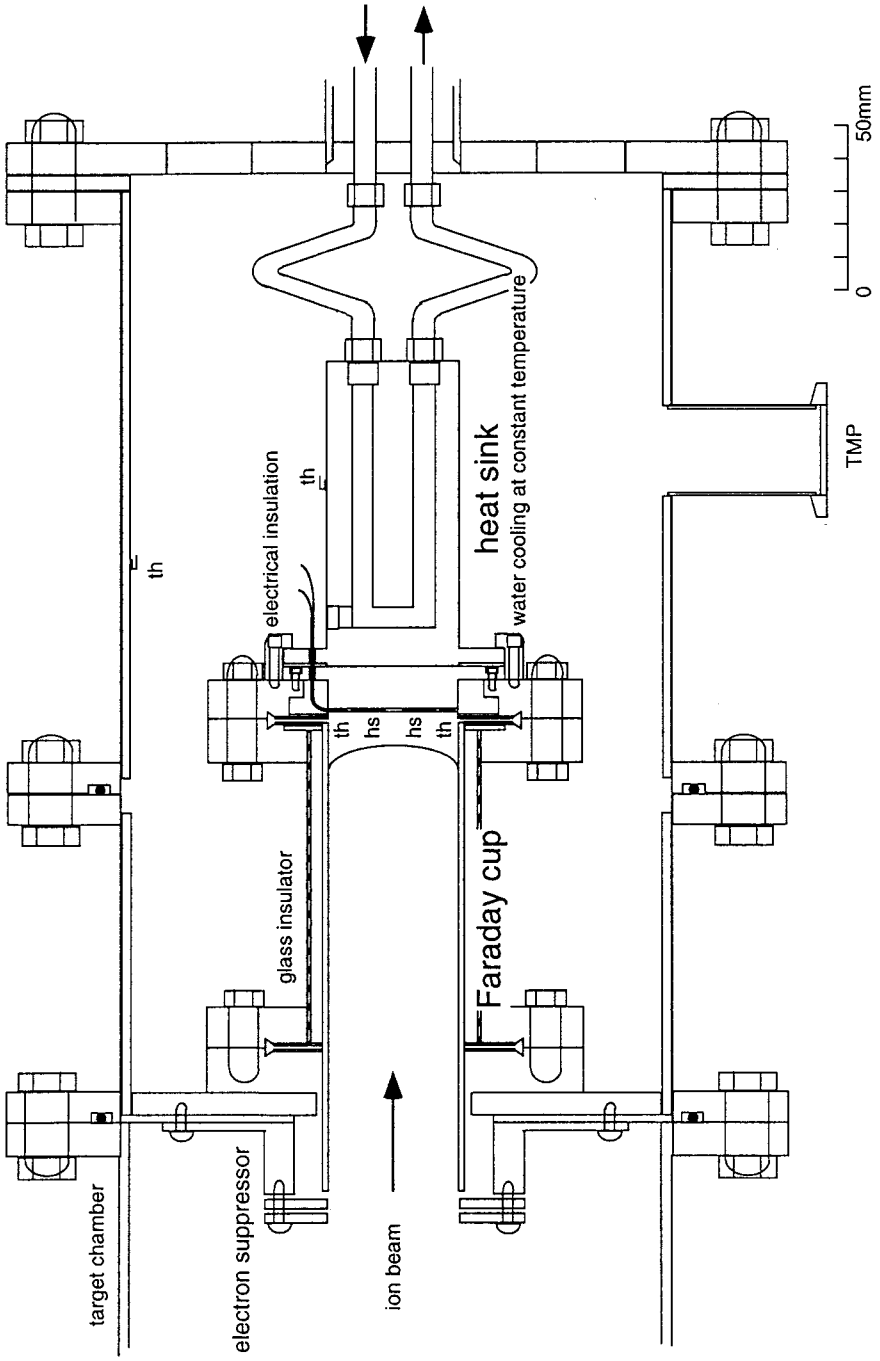

Figure 13: Cross sectional view of the beam calorimeter. The symbol "hs" represents the heat flux sensor and "th" represents the thermistor sensor.

can also measure the the number of incident particles by an electrical method, when the target chamber is in vacuum. At the entrance of the Faraday cup, the secondary electron suppressor is installed. To precise measurement by the electrical method, it suppresses secondary electrons caused by an interaction between the beam and the Faraday cup surface.

In this calorimeter the heat flux sensor (OMEGA HFS-3) is primarily used to measure a heat flow from the Faraday cup to the heat sink. Between the Faraday cup and the heat sink, two heat flux sensors are sandwiched with thermistor temperature sensors. They are originally insulated electrically. The absolute calibration between the heat flow and beam current is detailed in the following section.

2.5.2 Beam intensity calibration

The beam intensity measurements by calorimetric method were calibrated by electrical measurement of the beam current keeping a target chamber in a vacuum. The relation between an incident beam current(I) and a heat flux(H) which is transferred through the HFS can be written as,

$$I \cdot \delta t = k_1 \cdot H \cdot \delta t + C \cdot \delta T, \tag{14}$$

where T is the temperature of the calorimeter and C is the heat capacitance of the Faraday cup. This equation shows that if the current I is changed, the converted heat is both used to heat the Faraday cup(second term of right hand) and is transfered to the heat sink(first term of right hand). The temperature difference between the Faraday cup and heat sink is larger, the transferred heat may also be large. Thus the second term $C \cdot \delta T$ can be rewritten as $k_2 \cdot \delta\ H$. And the equation (14) can be written as,

$$I = k_1 \cdot H + k_2 \frac{\delta H}{\delta t}. \tag{15}$$

In order to determine the parameters k_1 and k_2, the experiment was made using a $^3He^{2+}$ beam of 40 keV. By the way during the experiment, to manipulate the beam into the central part of the bottom of the Faraday cup, the non-neutral part of the $^3He^{2+}$ ion beam is significantly useful. Since a measured beam current is stable, it is naturally to assume that a fluctuation of the beam current does not significantly affect the response function between the current and the heat flux output. The beam current was calculated directly from the HFS output by comparison with the Faraday cup indications. The parameter k_1 and k_2 can be determined as follows:

(1)*Parameter* k_1 *:* If the system is stable, i.e., incident beam I and T is stable, the second term of the equation (15) can be ignored. In this condition, the parameter k_1 can be derived as shown in Fig. 14.

(2)*Parameter k_2:* Parameter k_2 can be also derived from the equation (15) once parameter k_1 is derived. Here, the term $\delta H/\delta t$ was estimated for averaging time intervals such as 3, 7, 15 and 30 sec, respectively. It was found that most suitable time interval was 30 sec. Fig. 15 shows $\delta H/\delta t$ as a function of $I - k_1 \cdot H$.

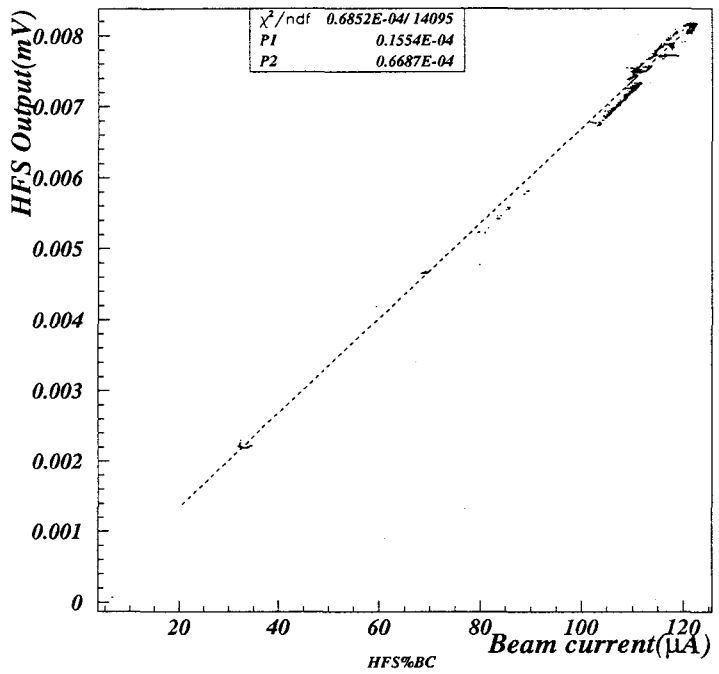

Figure 14: Relation between the beam current($I(\mu$A)) and the heat flux(H (mV)), with a condition of the second term in Eq.15 $\delta H/\delta t = 0$.

(3)*Comparison with beam current :* Fig. 16 shows the beam current as a function of time, measured by an electric and by the calorimetric methods ($k_1 \cdot H$, and $k_1 \cdot H + k_2 \frac{dT}{dt}$) under different conditions. When the beam current is stable, slowly increased or decreased, calculated currents measured by HFS well reproduce the ones measured by the Faraday cup as shown in Fig. 16 a), b) and c). On the other hand, when the beam current changes with stepwise(Fig. 16 d)), calculated currents seems to be over-emphasized compared with the one measured by HFS. Fig. 17 shows the accuracy of the calculated beam current with beam current in the form of $(I(HFS) - I(FC))/I(FC)$, where I(xx) is the beam current measured by

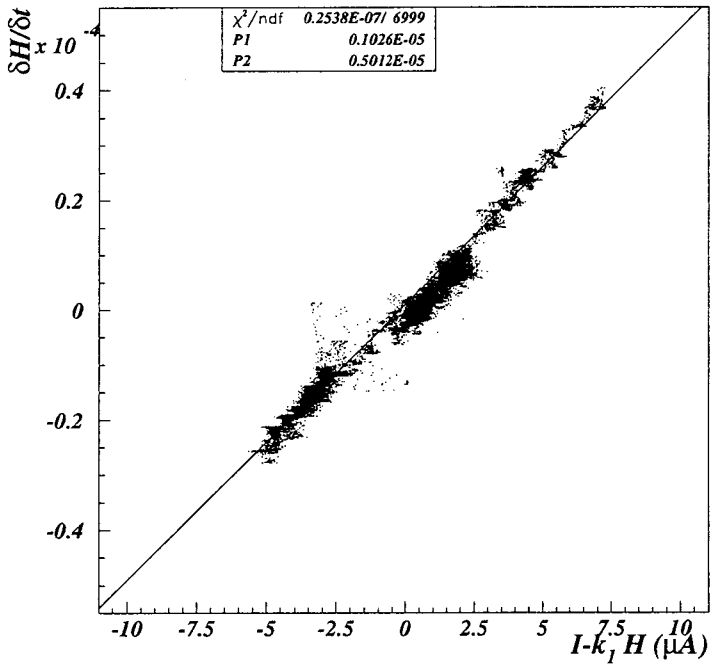

Figure 15: Relation between the difference of $I - k_1 \cdot H$ and first order differential of $\delta H/\delta t$(Eq. 15 in text).

HFS and Faraday cup(FC). In the calculation for an agreement of the calibration, the accuracy of beam current obtained by HFS is about 2% at most.

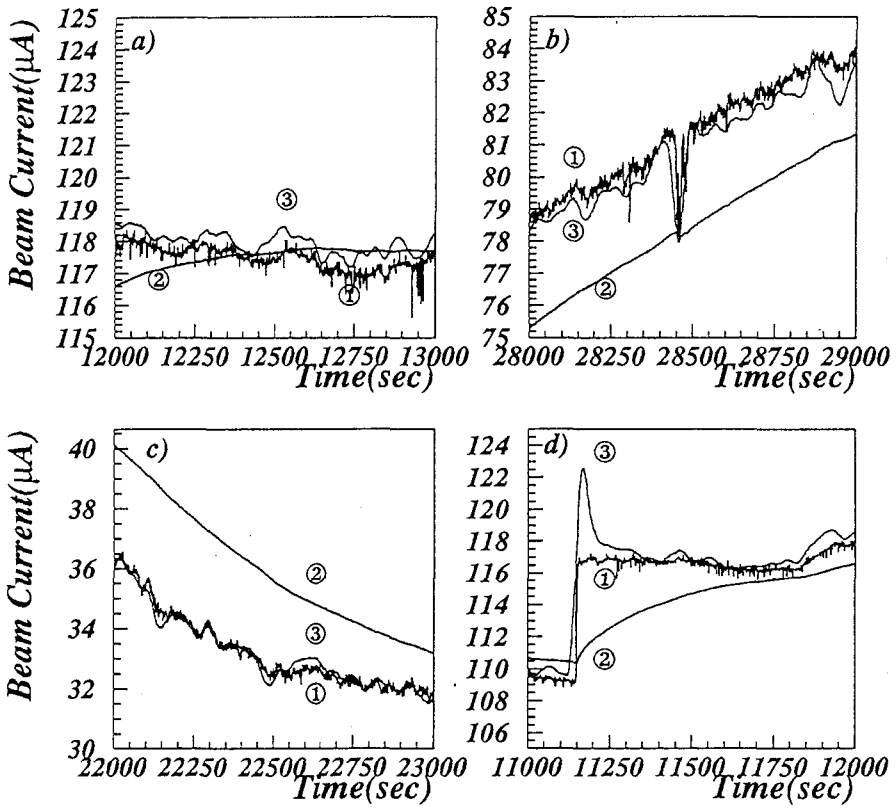

Figure 16: Beam current, measured by Faraday cup ①, calculated from $k_1 \cdot H$ ②, and $k_1 \cdot H + k_2 \cdot \delta H/\delta t$ ③ as function of time. Measurements were made for a) stable beam current, b) increasing beam current, c) decreasing beam current, d) beam current changing with stepwise.

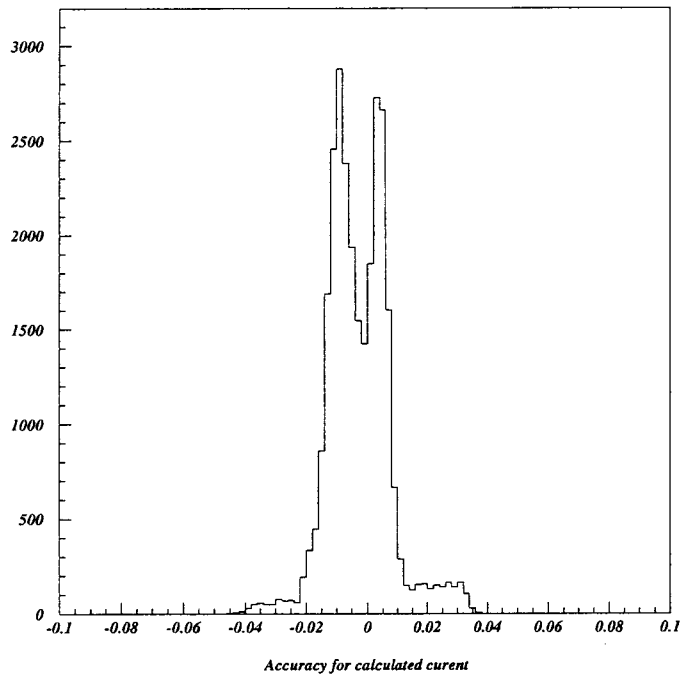

Figure 17: The accuracy of the calculated beam current in the form of $(I(HFS) - I(FC))/I(FC)$, where I(xx) denotes the beam current measured by HFS and Faraday cup(FC).

2.6 ΔE-E counter telescope

A detection efficiency and a clear discrimination of the real event from a background are substantial for the measurement of the rare events for the ^{3}He(^{3}He,2p)^{4}He reaction at low energy region. The semiconductor detector counting telescope for ΔE, E measurements has to have a large active area compared with that used for usual nuclear reaction measurement. The telescope is useful for considerable reduction of the background event rate arising from the d(^{3}He,p)^{4}He reaction, electrical noise and cosmic rays.

2.6.1 Detector configuration

The ^{3}He(^{3}He,2p)^{4}He reaction has a Q-value of 12.86 MeV, and it generates two protons which have kinetic energies of $0 \sim 10.7$ MeV, and an alpha particle which has kinetic energies of $0 \sim 4.3$ MeV. To identify the reaction in OCEAN facility, the silicon ΔE-E counter telescope is installed in the gas target to measure the energy of the proton(Fig. 18). To get the large detection efficiency, ΔE-counter and E-counter have a large active area (50 mm × 50 mm). The ΔE-counter has a thickness of 140 μm and the E-counter has a thickness of 1500 μm. They were provided by MICRON SEMICONDUCTOR Ltd. An aluminized Maylar films with thickness of 25 μm are installed in front of all ΔE-counters, to stop the generated alpha particle and elastic ^{3}He from the beam. Four set of ΔE-E counters are installed surrounding the beam-target interaction region symmetrically. The distance between the ΔE-counter and the beam axis is 32.5 mm and the distance between the E-counter and the axis is 37.1 mm. These distances are as short as possible to increase the detection efficiency.

2.6.2 Data acquisition system

Standard NIM electronics was used in connection with the ΔE-E counter telescope. The schematic view of the data taking system is shown in Fig. 19. Analog signals from each detector are fed into preamplifiers (model 142IH, ORTEC, for ΔE-counter and model 142B, ORTEC, for E-counter) which are installed near the target chamber. The shorter distance between the detector and preamplifier is desirable to reduce an electrical noise. Restricted geometrically, this distance is 45 cm. The signals from the preamplifiers are amplified by both spectroscopy amplifiers(S-AMP, model 472, ORTEC) and timing filter amplifiers (TFA, model 454, ORTEC). The

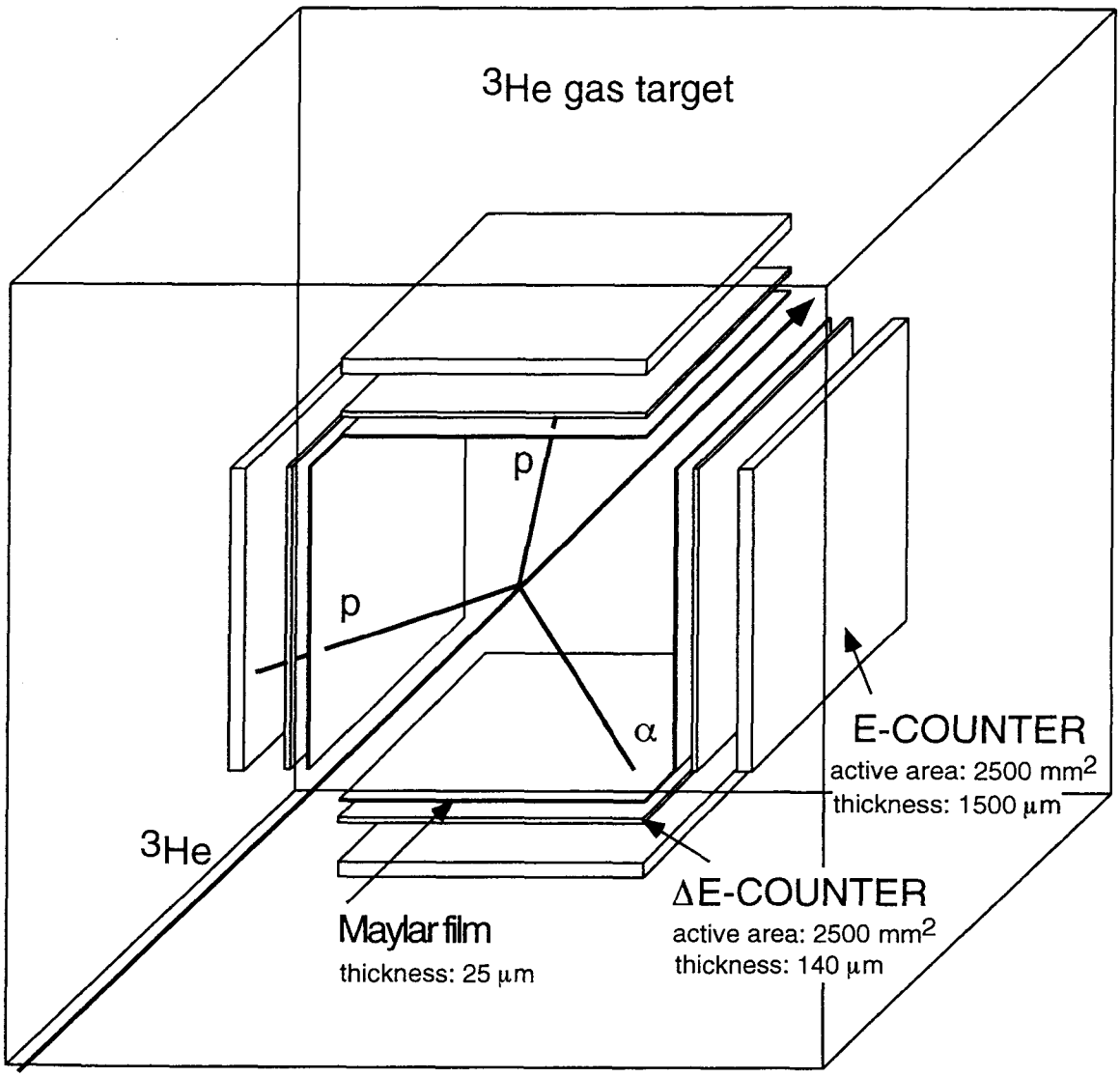

Figure 18: ΔE-E counter telescope

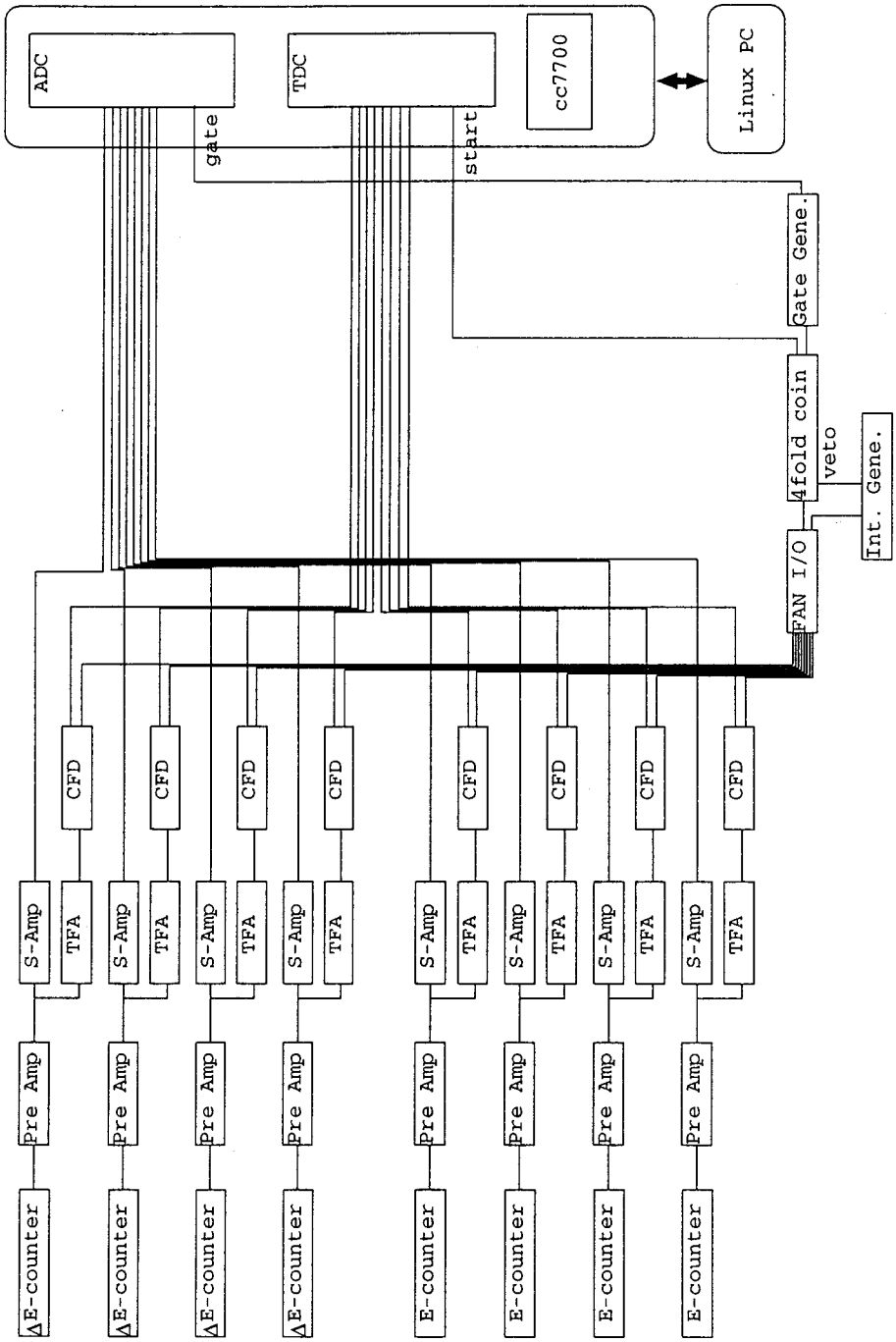

Figure 19: Schematic view of the data taking system

signals from the S-AMP are led to a CAMAC peak sensitive analog-digital-converter system(ADC, model AD811, ORTEC) and the signal from the TFA are led to a system of constant fraction discriminators(CFD, model 935, ORTEC), where threshold above the noise level of the detectors is set. The logic output of the CFD is fed into an logic Fan-In/Fan-Out(Fan-I/O, model 429A, ORTEC) delivering a gate signal for the CAMAC ADCs with the gate width of 400 nsec. Also the logic output provides a start signal for a time spectrum via a CAMAC time-digital-converter system(TDC, model 2228A, ORTEC). The stop signal of the TDC is provided also by the CFD with an delay time of 100 nsec. The signals from the ADC and TDC systems are delivered to a CAMAC crate controller(model CC7700, TOYO). Via a CAMAC bus, the data from the crate controller is transferred to a Linux station(model L400c, DELL) and stored on disk in the PAW package format.

The dead time of this data taking system is 400 μsec for 1 event. Typical counting rate of the measurement of ^{3}He+^{3}He reaction which includes the background events caused by ^{3}He+d reaction, cosmic rays, and electrical noise, is usually about 3 counts/sec. Therefore, the total dead time of these measurements is about 0.1 %.

2.6.3 Energy calibration

As it is well known that, the response of a Si detector is independent on the particle type for light ions, all the counters were calibrated by ^{241}Am α source(5.48 MeV). The energy spectrum of the calibration is shown in Fig. 20. Energy resolution of ΔE-counters was 100 $\sim$ 120 keV(FWHM) at 5.48 MeV of α particle, and those of E-counter was 70 $\sim$ 100 keV(FWHM), respectively. The energy gain of S-AMP was optimized to be able to measure the energy range up to 10 MeV for the ΔE-counter and 20 MeV for the E-counter, respectively . This energy range is required to measure not only ^{3}He+^{3}He events but also ^{3}He+d events, because ^{3}He+d events are needed for estimation of background and they are useful for check of energy calibration.

The linearity of the electrical circuits was measured by use of a precision pulse generator(model 419, ORTEC). The result for ΔE-counter is shown in Fig. 21. In these data the range of axis corresponds to the energy range of ΔE-counter(0$\sim$10 MeV). The linearity is within 0.05 % for all of the energy range of each counter.

The stability of energy gain of the preamplifier and the S-AMP were checked by the pulse generator before and after each measurement. The resultant gain shifts were less than 2 % for 6 months.

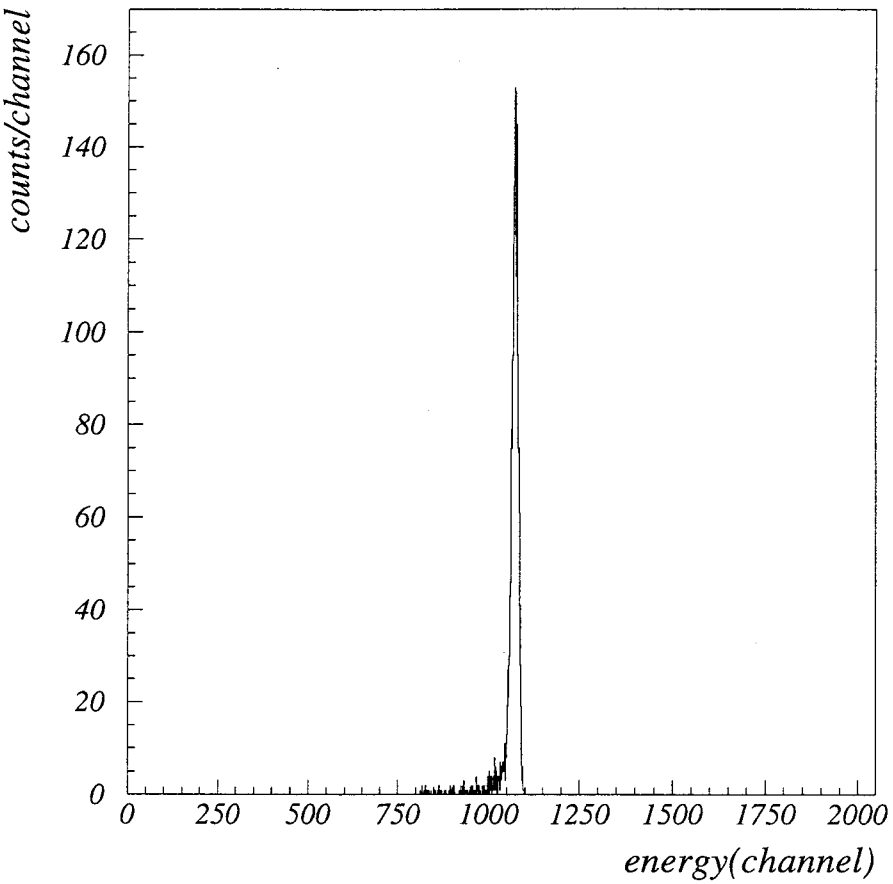

Figure 20: Typical ^{241}Am energy spectrum of ΔE-counter. The energy resolution is 102 keV(FWHM) at 5.48 MeV.

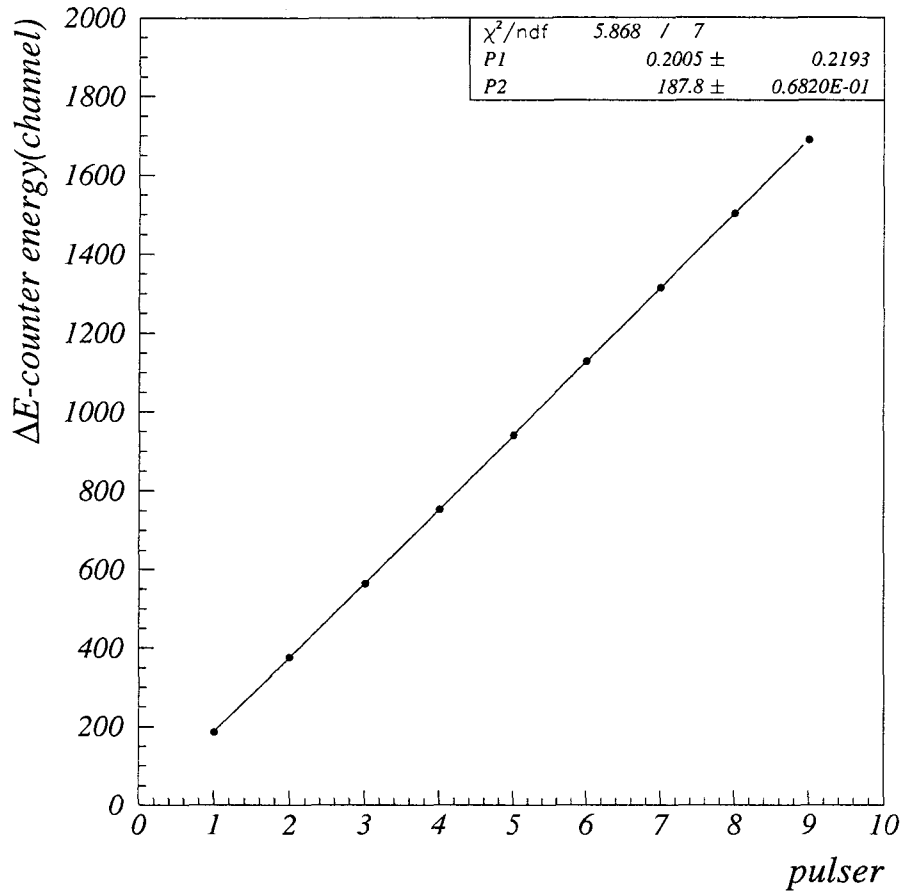

Figure 21: Linearity of the electrical circuit for the ΔE-counter. The range of axis corresponds to the energy range of 0 $\sim$ 10 MeV for ΔE-counter. The linearity is within 0.05 % for all of the energy range of each counter.

3 Experimental Result and Analysis

The number of counts $dN(z)$ per unit of time arising from a differential length dz of the extended ^{3}He gas target is given by the expression

$$dN(z) = N_t \cdot N_b \cdot \sigma(E(z)) \cdot \eta(z) \cdot dz, \tag{16}$$

where

$N(z)$—number of counts for ^{3}He(^{3}He,2p)^{4}He reaction,
N_t —^{3}He target density,
N_b —^{3}He beam intensity per unit of time,
$\eta(z)$ —the absolute detection efficiency.

Introducing the stopping power ϵ (i.e. the energy loss per unit length), Eq.(16) can be rewritten in the form

$$dN(E) = N_t \cdot N_b \cdot \sigma(E) \cdot \eta(E) \cdot \epsilon(E)^{-1} \cdot dE. \tag{17}$$

The total number of counts for the full target length is then given by

$$N = N_t \cdot N_b \cdot \int_L \sigma(E) \cdot \eta(E) \cdot \epsilon(E)^{-1} \cdot dE. \tag{18}$$

For the case of a thin target, introducing an effective reaction energy E_{eff} corresponding to the mean value of the projectile energy distribution in the detection setup, one arrives at

$$N = N_t \cdot N_b \cdot \sigma(E_{\text{eff}}) \cdot \int_L \eta(E) \cdot \epsilon(E)^{-1} \cdot dE. \tag{19}$$

For evaluation of the cross section, the number of counts for ^{3}He(^{3}He,2p)^{4}He reaction, the ^{3}He target density and the ^{3}He beam intensity should be measured. The values for the effective reaction energy and the integral term for detection efficiency were derived from the Monte Carlo program developed in frame of the present work.

3.1 Effective reaction energy

The effective reaction energy was derived from the beam energy considering the energy loss in the target gas.

3.1.1 Beam energy

The absolute beam acceleration voltage which was divided with a ratio of 1/10000 by the resistive voltage divider, was measured by the digital multi-meter with an accuracy of 0.1 % as mentioned in Sec. 2.2.2. It was measured at intervals of 1.5 second for all measurements. The stability of the voltage measured for about one day, is shown in Fig. 22. The energy spread of 0.005 % due to the change of the

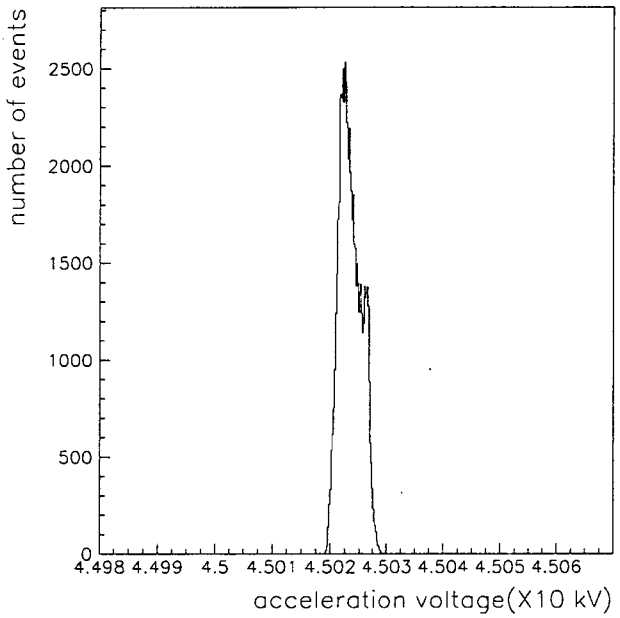

Figure 22: Measurement of the acceleration voltage at the beam extraction system. The data were measured at intervals of 1.5 sec for about one day. The derived energy spread due to the change of the acceleration voltage was 0.005 %.

acceleration voltage is negligible as shown in Fig. 22.

3.1.2 Energy loss in the target

For the calculation of the energy loss in the target gas, stopping power values given by the SRIM computer program [60, 61] were used. It should be pointed out

that experimental energy loss data [62] at the low energies were found consistent with those from the SRIM program, within the experimental error of 10 %. We adopted this error in our analysis.

Let us consider the case of an incident ^{3}He energy of E_{lab}=90.0 keV which can be measured with an accuracy of 0.1 % as discussed above. The stopping power given by the SRIM program at E_{lab}=90.0 keV is 9.3×10^{-15} eV/atom/cm^2. The reaction energy distribution in the target simulated by the Monte Carlo program, is shown

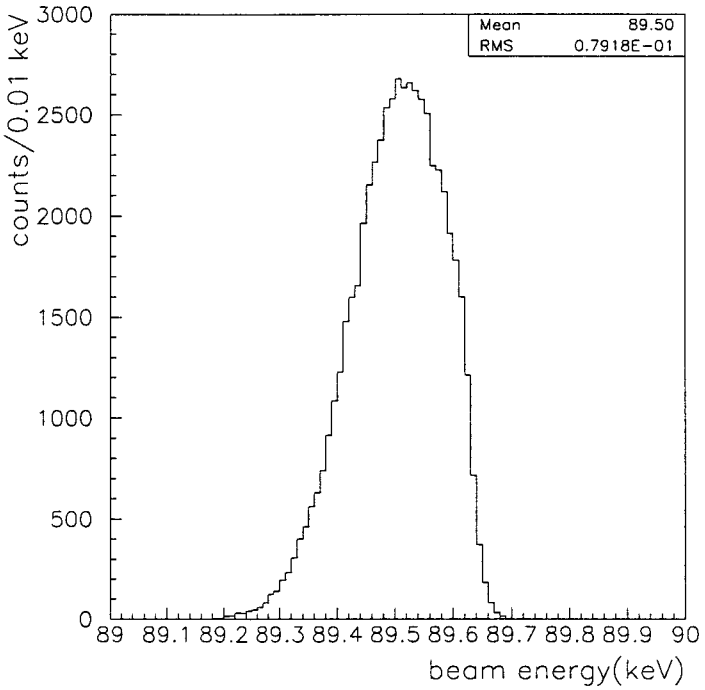

Figure 23: Simulated reaction energy distribution for the ^{3}He(^{3}He,2p)^{4}He reaction at an incident beam energy of E_{lab}=90.0 keV. The target gas pressure of 0.1 Torr is assumed.

in Fig. 23. The distribution corresponds to the integral in Eq. (19);

$$\int_L \eta(E) \cdot \epsilon(E)^{-1} \cdot dE,$$

where $\eta(E)$ is the detection efficiency and $\epsilon(E)$ is the stopping power. In this calculation we put the following parameters as:

- E_{lab}=90.0 keV for an incident beam energy,
- p=0.1 Torr for a pressure of the ^{3}He gas target,
- L=30 cm for the distance between the entrance of the target which corresponds to the entrance of the collimator C (see Fig. 12) and the entrance of the beam calorimeter on beam axis,
- ϵ=9.3×10^{-15} eV/atom/cm^2 for the stopping power for the ^{3}He beam of 90.0 keV given by the SRIM.

In addition, the effect of the rapid reduction of the cross section caused from the small energy loss in the target gas was estimated. For a constant $S(E)$ factor, the cross section drops by 11.2 % over the target thickness of 30 cm. From the mean value of this energy distribution as shown in Fig. 23, the effective energy loss in the target is evaluated to (500 ± 50) eV. By hand calculation, the energy loss between the entrance of the collimator C and the center of the counter telescope on the beam axis is 493 eV, which is in agreement with simulated one.

The energy spread in Fig. 23 is caused by the effective target length seen from the ΔE-E counter telescope as shown in Fig. 24. In this figure, the value of the zero of x-axis represents the center of the telescope on the beam axis. The effective target length is not symmetrical as expected by geometrical considerations. The energy spread in the target is estimated to 79 eV, which is considered as the error of E_{eff}.

An energy loss in the three pumping stage between the ion source and the entrance of the target has been also estimated. Assuming the incident beam energy of $E_{\rm lab}$=90.0 keV and using the stopping power for the beam energy, the energy loss is calculated to (3.3 ± 0.33) eV, which value is 3.7×10^{-3} % of incident beam energy.

To summarize, at an incident beam energy of (90.0 ± 0.090) keV, the effective reaction energy is evaluated to E_{lab}=(89.50 ± 0.13) keV, considering the accuracy of 0.1 % for the acceleration voltage, 10 % for the stopping power and 0.09 % for the energy spread in the target.

3.2 Beam intensity

The ^{3}He beam intensity was measured by the calorimetric method as detailed in Sec. 2.5. The measured beam intensity should be corrected for the energy loss in the target gas, since the beam calorimeter was calibrated keeping the target chamber in a vacuum. The energy loss was calculated by SRIM program as discussed in Sec. 3.1.2. For an incident beam energy of 90.0 keV, the energy loss was evaluated

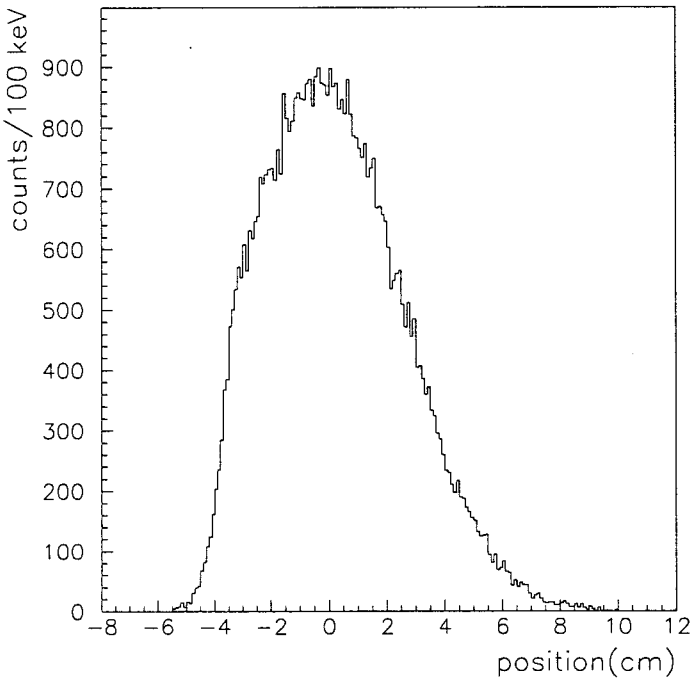

Figure 24: Simulated effective target length seen from the ΔE-E counter telescope. The zero of the position represents the center of the telescope on the beam axis.

to (1.60±0.16) keV, taking into account the distance from the collimator C (see Fig. 12) to the bottom of the beam calorimeter. As the result, the measured beam intensity was 1.8 % lower than the incident one.

The corrected beam intensity measured by the beam calorimeter is shown in Fig. 25. The intensity was simultaneously corrected by recording the beam energy

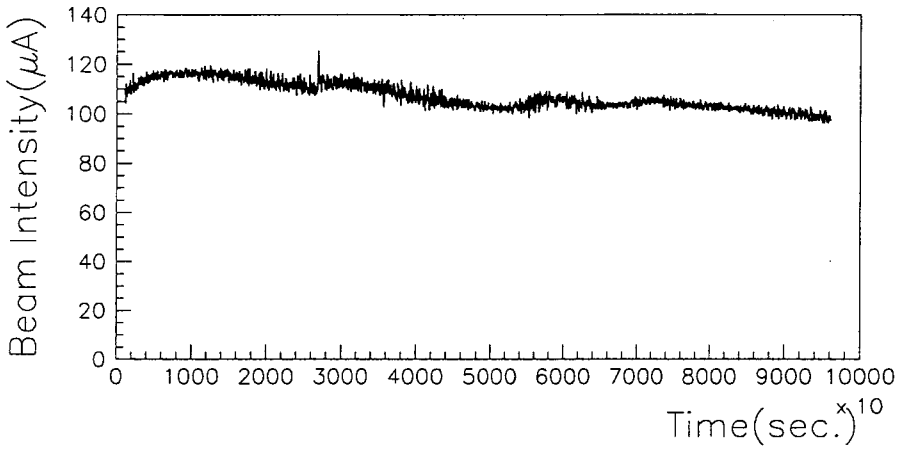

Figure 25: Measured and corrected intensity of ^{3}He beam at $E_{\rm lab}$=90.0 keV. Intervals of the measurement was 1.5 sec.

and the target gas pressure at intervals of 1.5 second. Typical beam intensity was about 100 μA at incident beam energy of 90 keV for $^3He^{2+}$ beam. As mentioned in Sec. 2.5.2, the beam intensity measured by the calorimetric method seems to be over-emphasized when the beam intensity changes with stepwise. Since the beam intensity was very stable, the correction for the over-emphasizing was not needed.

3.3 Target density

There are several factors which affect on the target density such as the gas temperature and a measurement point of the target gas pressure. The way how to correct the estimation of the target density due to these factors is explained in following sections.

3.3.1 Correction due to the target gas temperature

To derive the target density from the measured gas pressure, the data of the target temperature are needed basically. Since the target gas was heated by the ^{3}He beam and cooled by the cryo pump which was used for the gas purification system, the temperature was likely to be different from that of the laboratory. Therefore we should measure the temperature inside the target chamber.

During all measurements the thermistor(103AT-2) which was installed at the end of the target inside the chamber, measured the temperature with an accuracy of 1 % of reading, as shown in Fig. 26. The data show that the temperature was

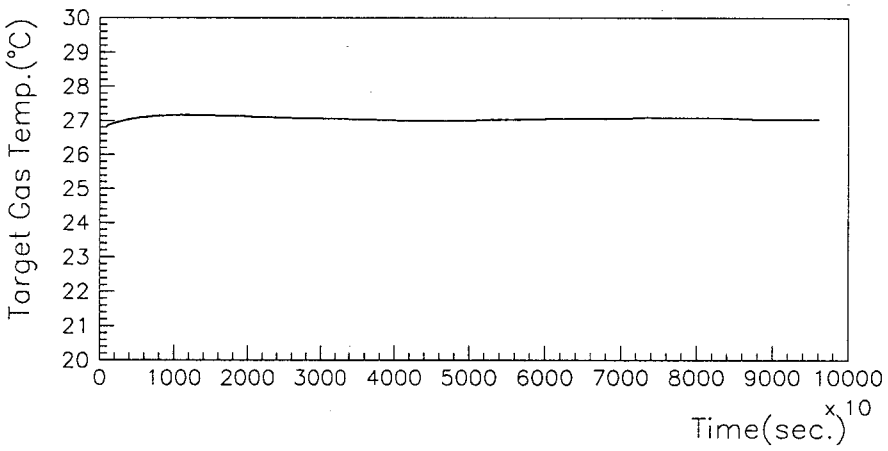

Figure 26: Temperature of the target gas during the whole time of the measurement. It was measured by the thermistor installed inside the target chamber with an accuracy of 1% of the reading.

very stable, and the value was close to that outside of the target chamber.

3.3.2 Correction due to the measurement position

During the experimental studies of the ^{3}He(^{3}He,2p)^{4}He reaction, we could not measure the target gas pressure at the beam-target interaction region. The pressure

was measured at the top of the target chamber as shown in Fig. 27. The measured gas pressure was likely to be different from that of the interaction region, because the region was surrounded by the various materials such as the four sided counter telescope, the detector holders, collimators and signal cables. Therefore, if there exists position dependence of the pressure inside the chamber, we should correct the measured gas pressure to that of the interaction region.

The gas pressure of the interaction region was measured by the extending stainless tube from the end of the target chamber. A schematic view of the measurement is shown in Fig. 27. The capacitance manometer which was usually installed at the

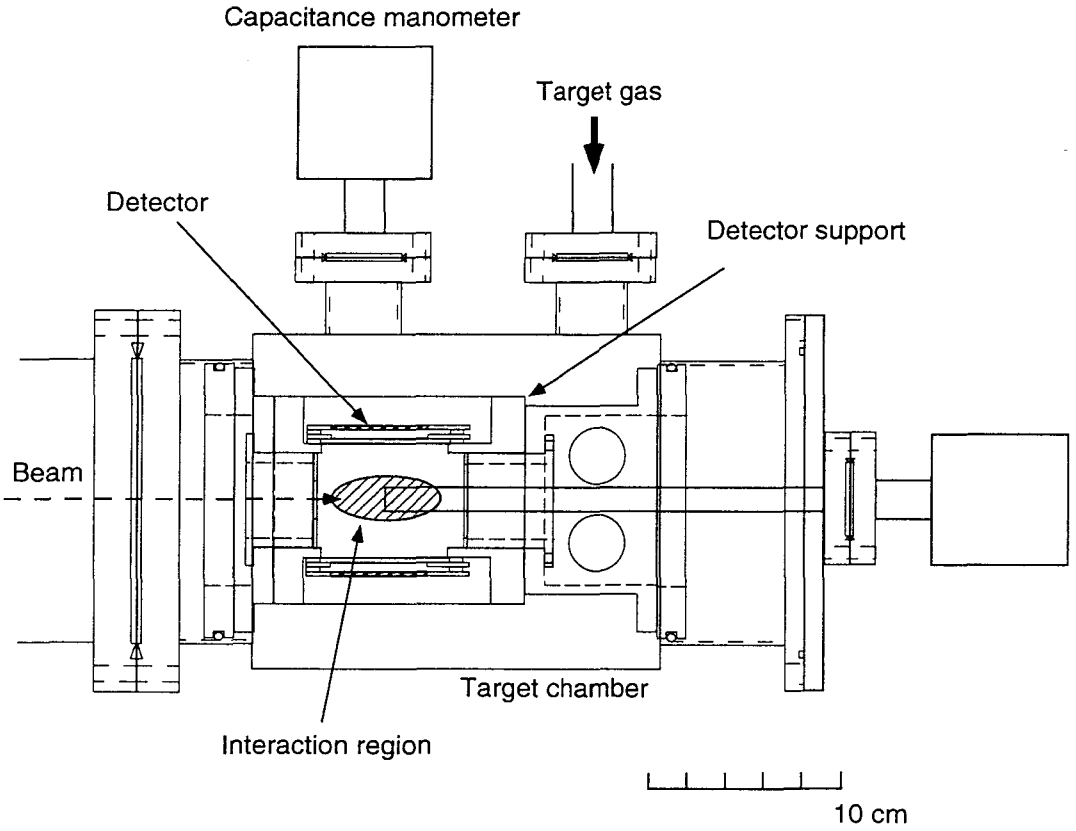

Figure 27: Schematic view of the measurement of the gas pressure at the interaction region between the beam and the target.

top of the target chamber, was removed to the end of the chamber. Simultaneously, we installed other gauge on the way of the gas circulation line for a normalization.

The relation between the target gas pressure at the top of the target chamber and that at the interaction region is shown in Fig. 28. The difference was found to

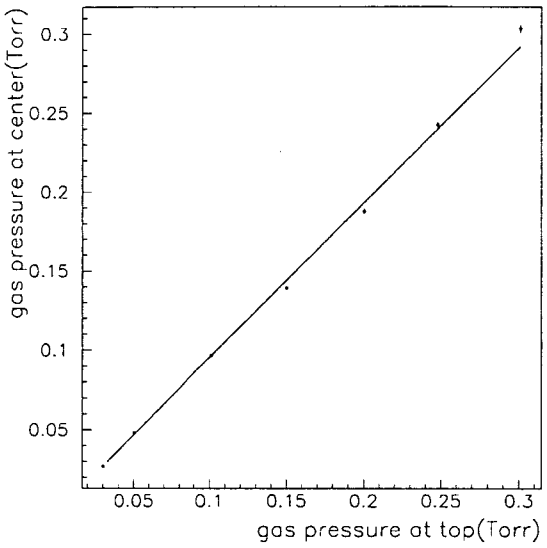

Figure 28: Relation between the target gas pressure at the top of the target chamber and at the interaction region. The pressure of the target gas was measured by the capacitance manometer at those two points as shown in Fig. 27, and normalized by use of other gauge.

be rather small, because the mean free path of 1.5 mm is shorter than the various free distance in the target chamber at the gas pressure of the order of 0.1 Torr. The target gas pressure at interaction region should be corrected 5 % less than that measured at the top of the target chamber.

Owing to these corrections, the target density can be determined to an accuracy of 1.3 %, considering the accuracy of 0.16 % for the measurement of the target gas pressure, 1 % for the correction due to the gas temperature and 0.8 % for the correction due to the measurement position.

The measured target gas pressure corrected as mentioned above, is shown in Fig. 29. The pressure was measured at intervals for 1.5 seconds. As mentioned in Sec. 2.4.2, the total amount of the ^{3}He gas in the windowless gas target system was regulated, since the ^{3}He gas flowed into the circulation line from the ion source steadily and it increased the gas pressure in the target. The target gas pressure had

a fluctuation of 20 %, since the regulation was carried out manually.

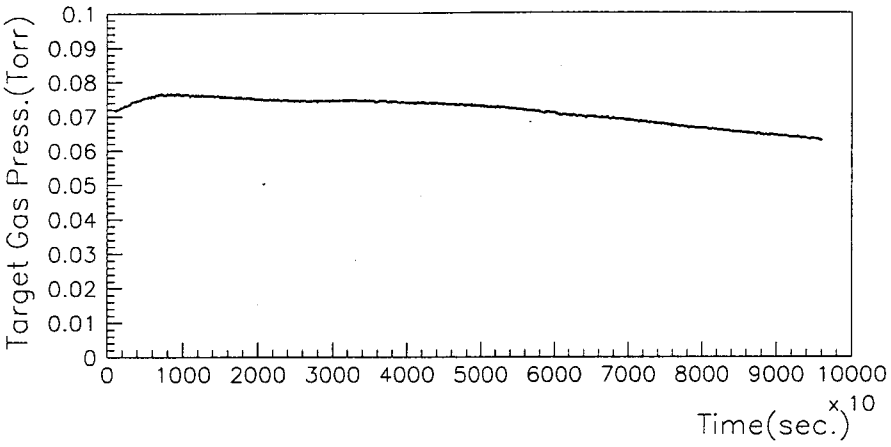

Figure 29: Measured target gas pressure by Baratron capacitance manometer. Intervals of the measurement was 1.5 sec. for all measurements for the ^{3}He(^{3}He,2p)^{4}He reaction. The pressure was normalized to that at temperature of 0 °C.

3.4 Data analysis

3.4.1 Monte Carlo simulation for OCEAN experiment

In order to optimize the detector setup and to estimate the absolute detection efficiency, a Monte Carlo program was written to simulate the detector response for ^{3}He(^{3}He,2p)^{4}He and for d(^{3}He,p)^{4}He reactions. The GEANT3 simulation code was used to calculate an interaction between the ejectiles from these reactions and the detectors. Also the GENBOD code of CERN library was used to generate the ejectiles. The simulation program takes into account the following aspects, such as:

- the geometry of the detectors, their thickness and their intrinsic energy resolution,

- the energy loss and energy straggling of the ejectiles in the target gas and in the film in front of the detectors,
- kinematic effects on the energies of the ejectiles in case of an extended gas target,
- yield dependence of the ejectiles on the cross section over the extended gas target.

The program produces energy spectra of the ejectiles for the detectors as well as absolute yields. The simulated spectra can be compared directly with experimental data.

3.4.2 Measurement of the d(^{3}He,p)^{4}He reaction

The d(^{3}He,p)^{4}He reaction(Q=18.4 MeV) was measured to verify of the written Monte Carlo program. This reaction was very useful for a test of a validity of the program because of the following reasons:

- the generated protons from ^{3}He+d reaction have a kinematically single energy of 14.7 MeV, therefore the interaction between these protons and detectors are evaluated easily;
- the protons from ^{3}He+d reaction have the similar energy of those from ^{3}He+^{3}He reaction(0$\sim$10.7 MeV), therefore the ^{3}He+d reaction can be measured by the detector setup developed for the ^{3}He+^{3}He measurement;
- the cross section of ^{3}He+d reaction is 10^6 greater than ^{3}He+^{3}He reaction, therefore the reaction has great deal event rate, which is necessary to test our simulation.

The d(^{3}He,p)^{4}He reaction was measured by the OCEAN facility used for the ^{3}He+^{3}He measurements. The energy of $^3He^{2+}$ beam was 90 keV and the beam intensity was 70 μA. The target pressure of the deuterium gas was maintained around 1.0×10^{-4} Torr, that was the minimum pressure controllable with a manual valve for a gas introduction into the chamber.

The observed energy spectrum for ΔE-E counter telescope is shown in Fig. 30. The broad structures observed at ΔE$\sim$1 MeV and E$\sim$5-14 MeV region arise from an insufficient depletion depth for protons which is incident on the detector at angle near 90° (see Fig. 31). In order to avoid a serious discharge in the gas target applying

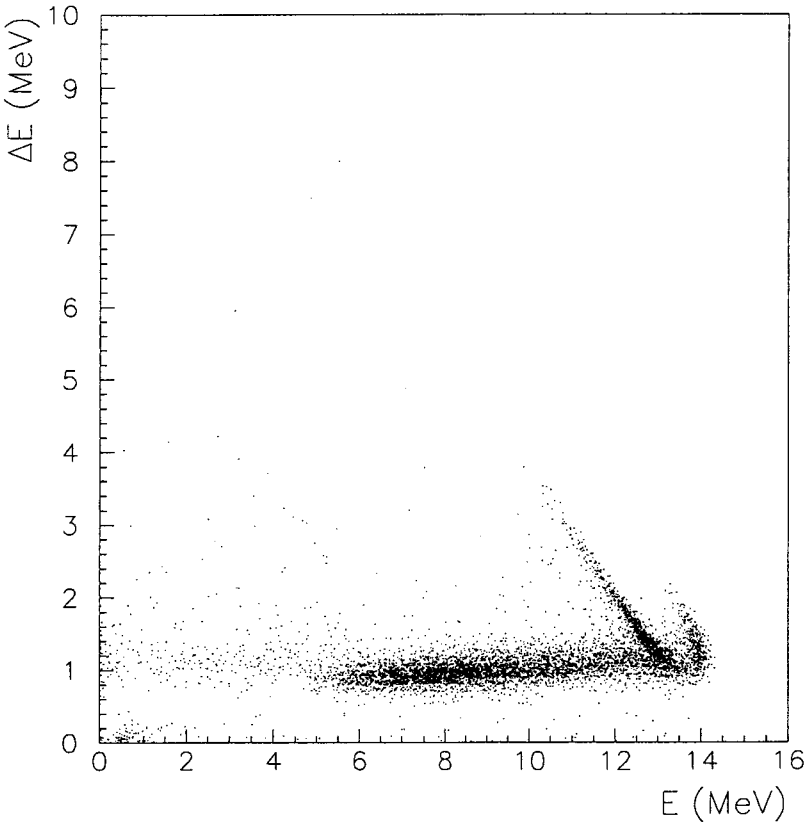

Figure 30: Observed energy spectrum of the ΔE-E counter telescope for the d(^{3}He,p)^{4}He reaction at $E_{\rm lab}$=90.0 keV.

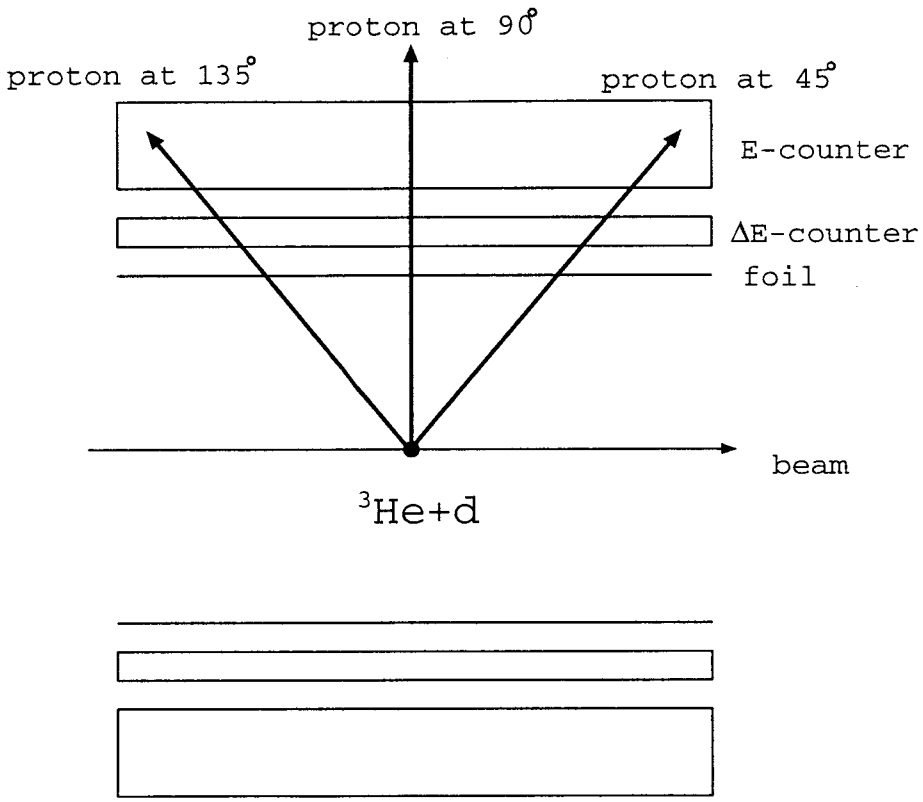

Figure 31: Schematic view of the d(^{3}He,p)^{4}He reaction. The protons of the incident angle near 90° can not stop in the E-counter completely, on the other hand, those of the incident angle of 0°-45° and 135°-180° stop.

the high bias voltage (more than 300 V, i.e. required for full depletion depth of E-counter) the energy spectrum of the d(^{3}He,p)^{4}He and ^{3}He(^{3}He,2p)^{4}He reaction were obtained with the bias voltage of 180 V which correspond to the depletion depth of 900 μm. In addition, there exists non-uniformity of the depletion depth for the E-counter as detailed below.

Other two structures arise from kinematic effects in combination with protons which are incident at angle range $135° - 180°$ and $0° - 45°$ on the detector, where they are stopped completely. These three remarkable structures are also shown in the simulated energy spectrum as shown in Fig. 32.

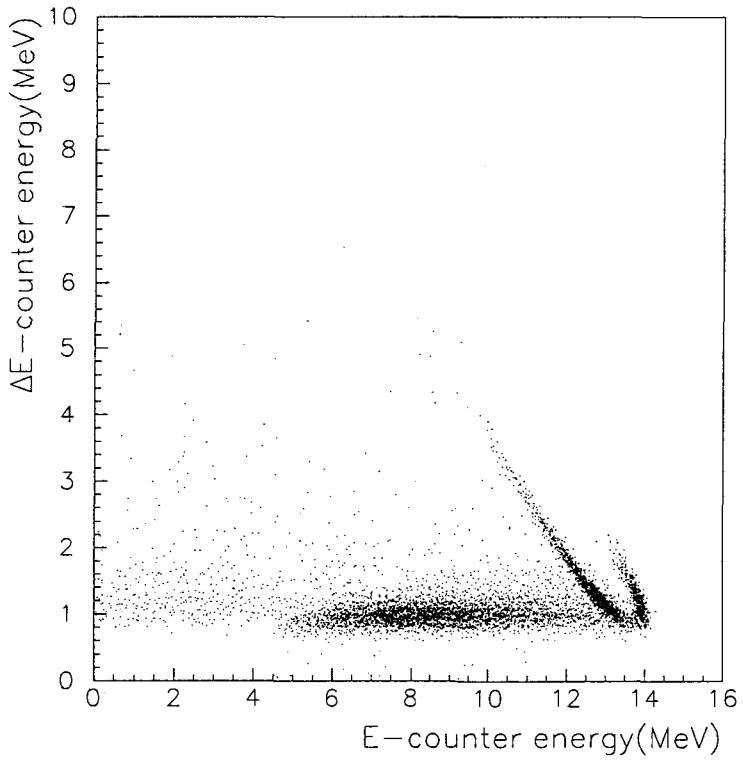

Figure 32: Simulated ΔE-E energy spectrum for the d(^{3}He,p)^{4}He reaction.

To compare the observed energy spectra with the simulated one more precisely, the observed and simulated energy spectra of the ΔE and the E-counter are studied separately.

For one of the ΔE-counters, the observed and simulated energy spectra are shown in Fig. 33. The observed spectra were obtained in coincidence with E-counter to

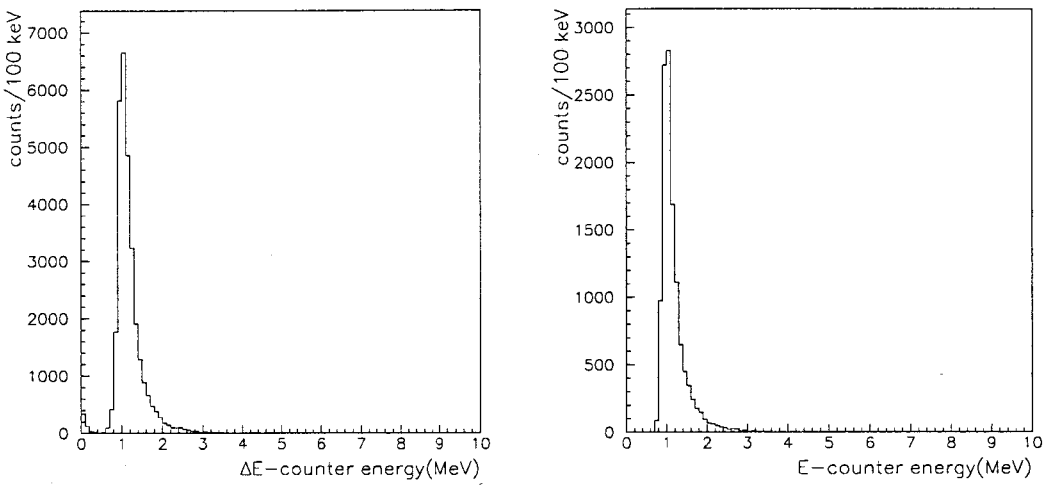

Figure 33: Observed(Left) and simulated(Right) energy spectrum of ΔE-counter for the d(^{3}He,p)^{4}He reaction.

reject the low energy background events caused by cosmic rays. In the case of the proton with an incident angle near 90° on the detector, the energy deposit is about 0.8 MeV, and the energy increases as the incident angle becomes larger. The simulated spectra is in a good agreement with the observed one.

For one of the E-counter, the observed and simulated energy spectra are shown in Fig. 34. The broad structure which can be seen around 8 MeV in Fig. 34, arises from the insufficient depletion depth for protons which are incident near 90° on the detector. The lower edge of the energy spectrum of the E-counter is determined by the minimum energy deposit of the proton which entered the E-counter at incident angle of 90°. The peaks at 12.8 and 13.8 MeV arise from the Doppler shift of protons which are incident at the angle range 135°-180° and 0°-45° on the detector, where they are stopped completely.

In Fig. 34, there seems to be a difference in the shape of structure especially of 6-8 MeV, between the measured and simulated spectra. In the measured spectrum, counts of protons depending on the energy, reduce gradually at the energy range 5-8 MeV, while the simulated energy distribution is reduced steeply. The difference is considered to be caused by the variety of the depletion depth. In the simulation, at

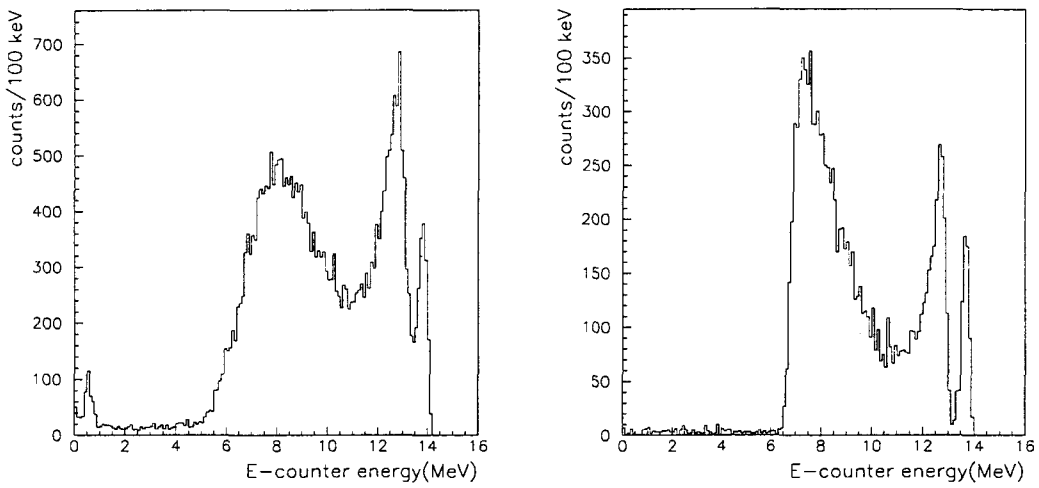

Figure 34: Observed(Left) and simulated(Right) energy spectrum of E-counter for the d(^{3}He,p)^{4}He reaction.

the first step, the thicknesses of depletion depths of ΔE and E counter are assumed to have a uniform thickness. In such the condition, the simulated energy spectrum of the ΔE-counter is in agreement with the observed one as shown in Fig. 33, while it causes the disagreement for the E-counter.

To investigate the distribution of the depletion depth of the E-counter, the measured energy spectrum of the E-counter with coincidence of energy window of the ΔE-counter between 0.8 and 0.9 MeV, were selected (Fig. 35). This energy spectrum corresponds to the distribution of the depletion depth of the E-counter, because the energy window of the ΔE-counter corresponds to the protons at incident angle near 90°. In this condition, the energy deposition of the proton in the E-counter is in proportion to the depletion depth, since the protons from d(^{3}He,p)^{4}He reaction have a single energy of 14.7 MeV. From the spectrum, we conclude that the present E-counter has non-uniform depletion depth which is distributed from 650 to 1200 μm. The simulated spectrum of the E-counter with the corrected depletion depth, is shown in Fig. 36. The simulated spectrum has a gradual slope at 5-8 MeV, and agrees with the measured one substantially.

In fact, the minimum thickness of the E-counter of 650 μm can completely stop the protons from the ^{3}He(^{3}He,2p)^{4}He reaction. Therefore, such distribution of the depletion depth does not affect to the studies for the ^{3}He(^{3}He,2p)^{4}He reaction.

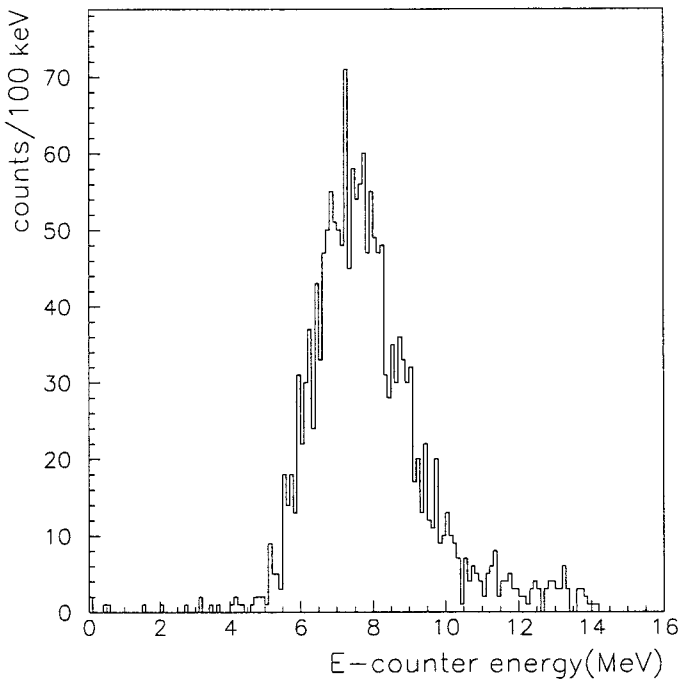

Figure 35: Measured energy spectrum of E-counter coincidence with the ΔE-counter between 0.8 and 0.9 MeV.

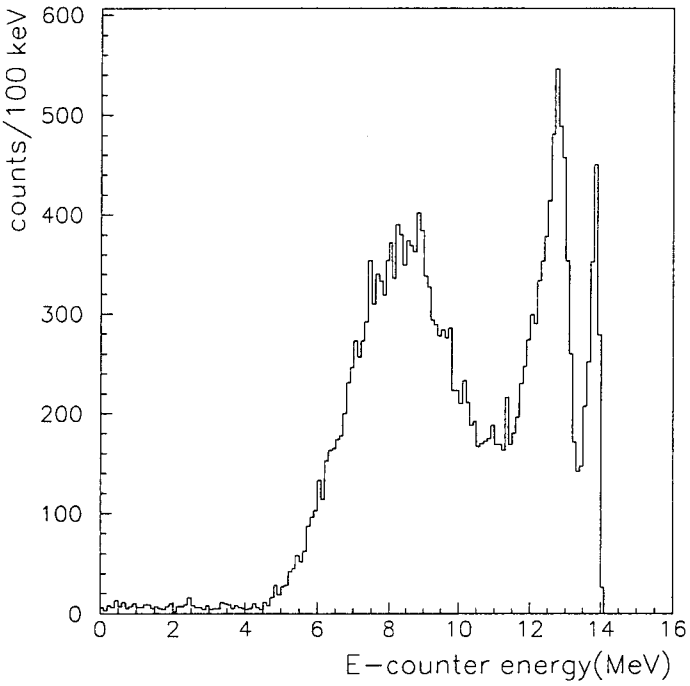

Figure 36: Simulated energy spectrum of E-counter. The assumed depletion depth is distributed from 650 to 1200 μm.

3.4.3 Background analysis

Deuteron contaminations both in the beam and the target gas are the most serious background origin, as mentioned in Sec.1.4. The contamination in the beam is in the form of mass-3 molecular ion HD^+ which can not be separated from the $^3He^{1+}$ ion by the present dipole magnet in the beam transport system. For this argument, if $^3He^{2+}$ beam is adopted for studies, it is not necessary to consider the intrusion into the beam. Then, we must only consider the contamination in the target gas.

The d(^{3}He,p)^{4}He events which arise from the deuterium contamination in the target gas can be distinguished as the background events in the ΔE-E scatter plot obtained by the measurement of the ^{3}He(^{3}He,2p)^{4}He reaction. The contamination level is evaluated from the events accepted as the d(^{3}He,p)^{4}He reacion events in the scatter plot specified in Fig. 37. Taking into account the detection efficiency

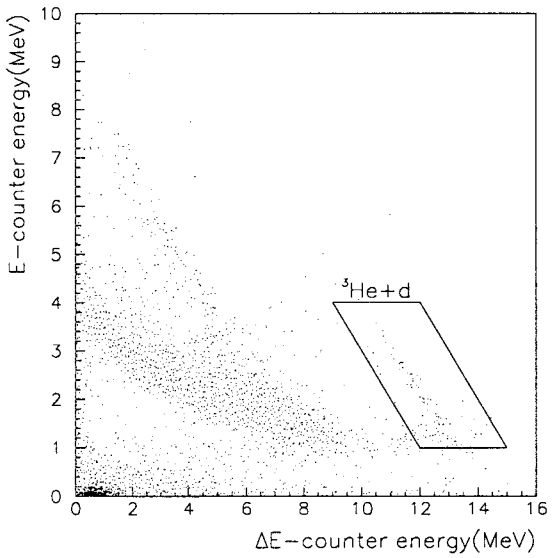

Figure 37: Observed ΔE-E energy spectrum of the ^{3}He(^{3}He,2p)^{4}He and d(^{3}He,p)^{4}He reaction. The solid line shows the acceptable energy region for the d(^{3}He,p)^{4}He events. The deuterium contamination in the target ^{3}He gas is evaluated from the events in this region.

derived from the Monte Carlo program as well as the cross section of the d(^{3}He,p)^{4}He

reaction in ref [58], we conclude that the contamination is 0.2 ppm of the target gas. It can be expected that in such contamination level, the background contribution at reaction energy of E_{cm}=45 keV, is less than 0.1 % of the observed ^{3}He(^{3}He,2p)^{4}He events.

Another source of background events arises from an electrical noise and cosmic rays. These background events were observed for 38 days. The result is shown in Fig. 38. The cosmic muon events are located around ΔE=70 keV and E=450

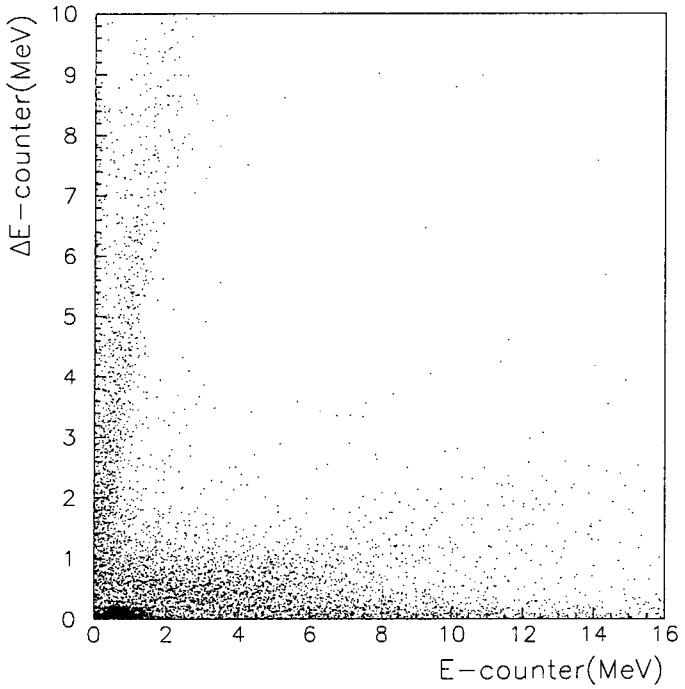

Figure 38: Background events arising from electrical noise and cosmic rays. They were observed with the same geometry as the ^{3}He(^{3}He,2p)^{4}He experiment.

keV, expected from the minimum ionization loss of 2 MeV·cm^2/g. The contribution of these background events is 3.6 counts/day in the acceptable region for the ^{3}He(^{3}He,2p)^{4}He reaction, which will be discussed later.

3.4.4 Analysis of ΔE-E scatter plots

The acceptable area in the ΔE-E scatter plot for the ^{3}He(^{3}He,2p)^{4}He reaction should be determined considering the signal-to-noise ratio(S/N). The origin of the background(Noise) events were assumed to be d(^{3}He,p)^{4}He reaction as well as the cosmic rays and the electrical noise. The energy distribution of ΔE (0∼10 MeV)-E (0∼16 MeV) counter telescope was divided into 16000 of 100 keV ×100 keV parts as shown in Fig. 39. For every part, S/N ratio was alloted and the parts which

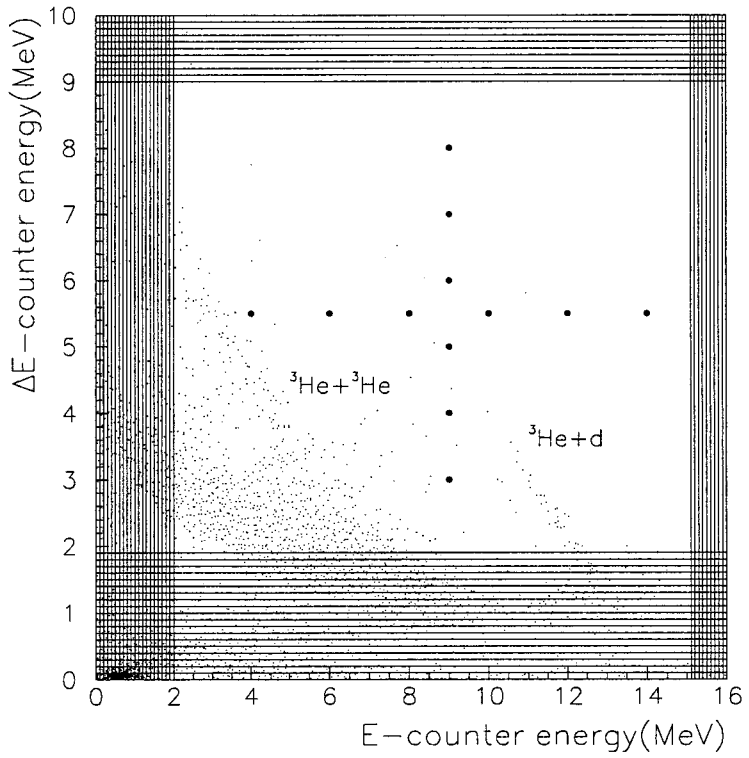

Figure 39: Schematic view of the analysis for the acceptable area for ^{3}He(^{3}He,2p)^{4}He events. The ΔE-E energy distribution was divided into 16000 of 100 keV ×100 keV parts. For every parts, S/N ratio was alloted respectively.

had better S/N ratio, were adopted for the acceptable area for the ^{3}He+^{3}He events. The distribution of ^{3}He+^{3}He (Signal) events in the scatter plot was simulated by

the Monte Carlo program. Also, the distribution of the ^{3}He+d events was simulated considering the deuterium contamination in the target gas derived from the accepted events as the d(^{3}He,p)^{4}He reaction in ΔE-E scatter plot (see Fig. 37). The allocation of other background components was obtained by the experimental background measurements. These background events were normalized by the live time of the ^{3}He+^{3}He reaction measurements. After the S/N ratio was estimated for every part of 100 keV $\times$ 100 keV, all parts were ordered again as a function of the S/N ratio to determine the acceptable area for the ^{3}He+^{3}He events.

The results of evaluation of the S/N ratio are shown in Fig. 40. Fig. 40(a) shows the distribution of the simulated ^{3}He+^{3}He reaction as the function of the S/N ratio. Many of the events are located in the right hand side in Fig. 40(a), corresponding to the better S/N ratio. Also, Fig. 40(b) and (c) show the distributions of the simulated ^{3}He+d reaction events and the observed other background events normalized as discussed above. These background events are located in the left hand side in each figures. Fig. 40(d) shows the distribution of the observed ^{3}He+^{3}He events at $E_{\rm cm}$=45 keV, as the function of the S/N ratio. In such an energy region, the contributions from these background events are very small. Therefore the observed distribution of the ^{3}He+^{3}He reaction is similar to the simulated one without any background subtractions.

From these analysis, most of the background events are found to be located in less than 13000 channel in Fig. 40. Therefore, the acceptable area for the ^{3}He+^{3}He reaction was determined over 13000 channel. The region is equivalent to the marked area in the ΔE-E scatter plot shown in Fig. 41.

In the case of the measurement for the ^{3}He(^{3}He,2p)^{4}He reaction at $E_{\rm cm}$=45.3 keV, 3344 counts is observed in the acceptable region, while the contribution of the ^{3}He+d events to the region, is estimated to 2.6 counts and that of the other background component is 4.0 counts. After the subtraction these background events from the acceptable events, the observed number of the ^{3}He+^{3}He events is 3337.4 counts, which corresponds to the statistical error of 1.8%.

The systematic error of the detection efficiency is estimated as follows. The error is caused by two components, the accuracy of the simulated ΔE-E energy distribution of the protons from the ^{3}He(^{3}He,2p)^{4}He reaction, and the accuracy of the geometrical parameter of the counter telescope for the Monte Carlo simulation.

The former accuracy is estimated from the fluctuation of the cross section depending on the acceptable region. The detection efficiency for the ^{3}He(^{3}He,2p)^{4}He reaction is derived from the summation of the simulated distribution over each cut

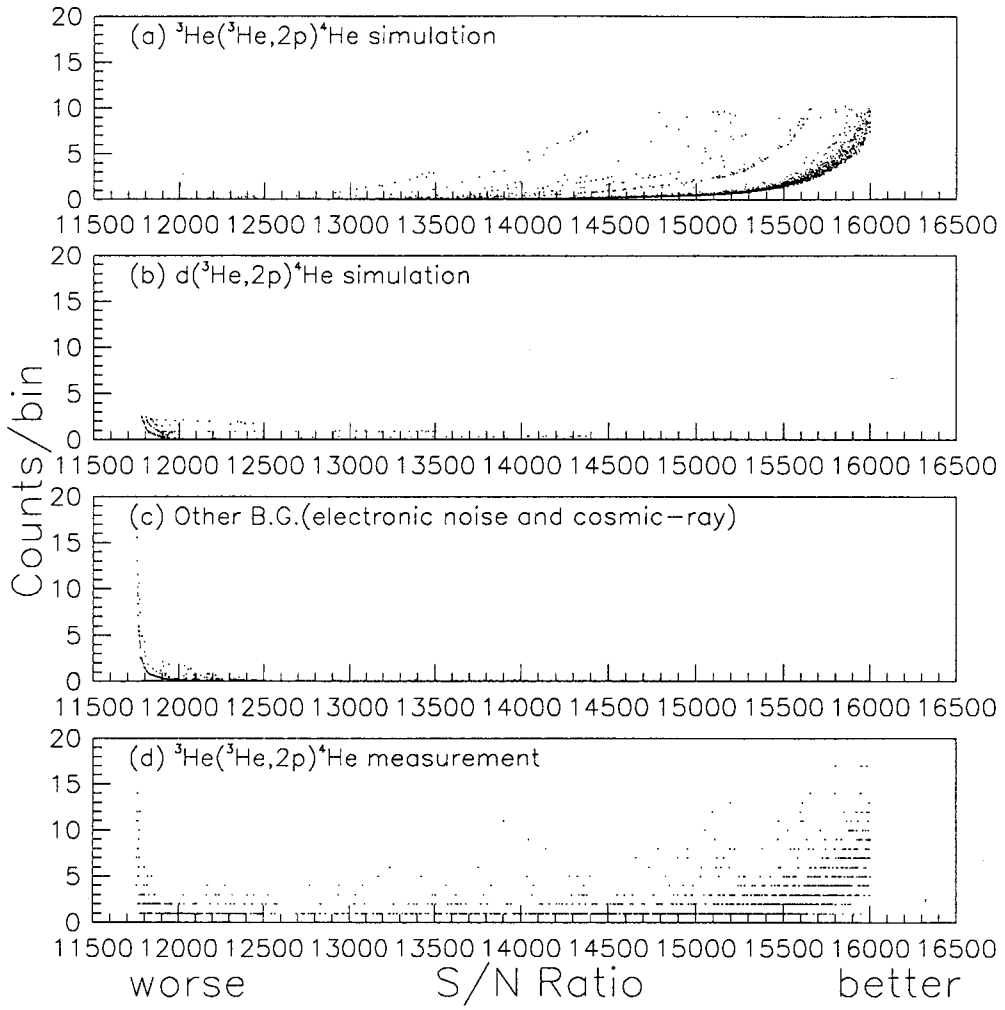

Figure 40: Distribution of each events depend on the S/N ratio. (a)simulated ^{3}He+^{3}He, (b)simulated ^{3}He+d, (c)observed other background(electric noise and cosmic-ray), (d)observed ^{3}He+^{3}He are shown. S/N is given by S(simulated ^{3}He+^{3}He)/ N(simulated ^{3}He+d + observed other background).

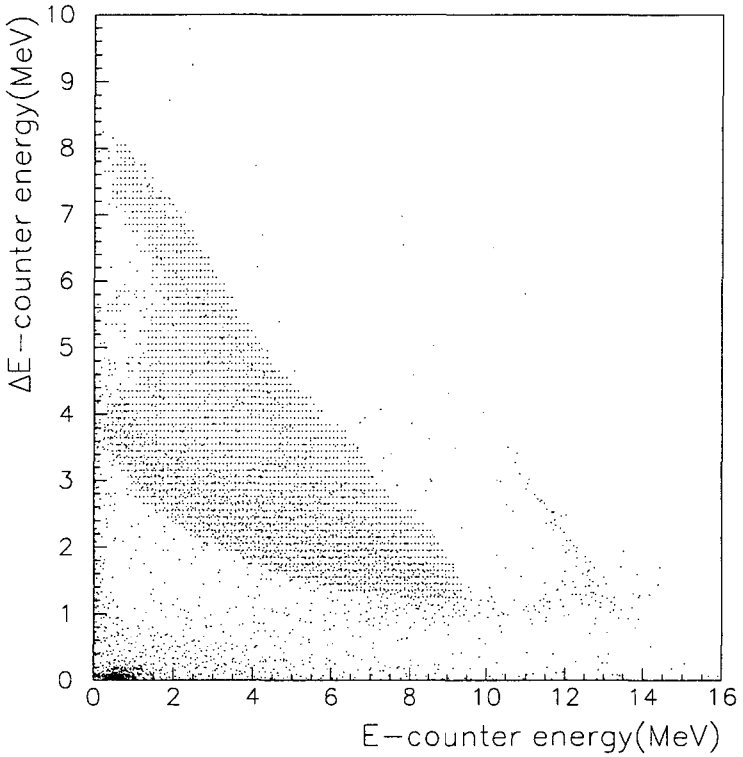

Figure 41: ΔE-E plot for the observed ^{3}He+^{3}He reaction. The marked area shown the acceptable region for the true events.

point in Fig. 40(a). It can be written as,

$$\eta(x) = \sum_{i=x}^{16000} N_{\mathrm{a}}(i), \tag{20}$$

where

$\eta(x)$ – detection efficiency for the ^{3}He(^{3}He,2p)^{4}He reaction,
$N_{\mathrm{a}}(i)$ – number of counts for the simulated distribution (Fig. 40(a)),
x – cut point (x axis in Fig. 40).

The accepted events for the ^{3}He(^{3}He,2p)^{4}He reaction are also derived from the summation of the observed distribution over each cut point in Fig. 40(d), considering the subtraction of the background events estimated as shown in Fig. 40(b) and (c), respectively. It can be written as,

$$A(x) = \sum_{i=x}^{16000} \{N_{\mathrm{d}}(i) - N_{\mathrm{b}}(i) - N_{\mathrm{c}}(i)\}, \tag{21}$$

where

$A(x)$ – accepted events for the ^{3}He(^{3}He,2p)^{4}He reaction,
$N_{\mathrm{d}}(i)$ – number of counts for the observed distribution (Fig. 40(d)),
$N_{\mathrm{b}}(i)$ – number of counts for the d(^{3}He,p)^{4}He distribution (Fig. 40(b)),
$N_{\mathrm{c}}(i)$ – number of counts for other background distribution (Fig. 40(c)).

The ratio of $A(x)/\eta(x)$ corresponds to the cross section of the ^{3}He(^{3}He,2p)^{4}He reaction. The ratio as a function of the cut point is shown in Fig. 42. From the fluctuation of this ratio due to a cut point, the accuracy of the simulated ΔE-E energy distribution of the protons from the ^{3}He(^{3}He,2p)^{4}He reaction, is evaluated to 3 %.

The accuracy of the geometrical parameter of the counter telescope for the Monte Carlo simulation is 0.1 mm, which corresponds to the 0.5 % of the detection efficiency. Summarizing these two components, the systematic error of the detection efficiency is evaluated to 3 %.

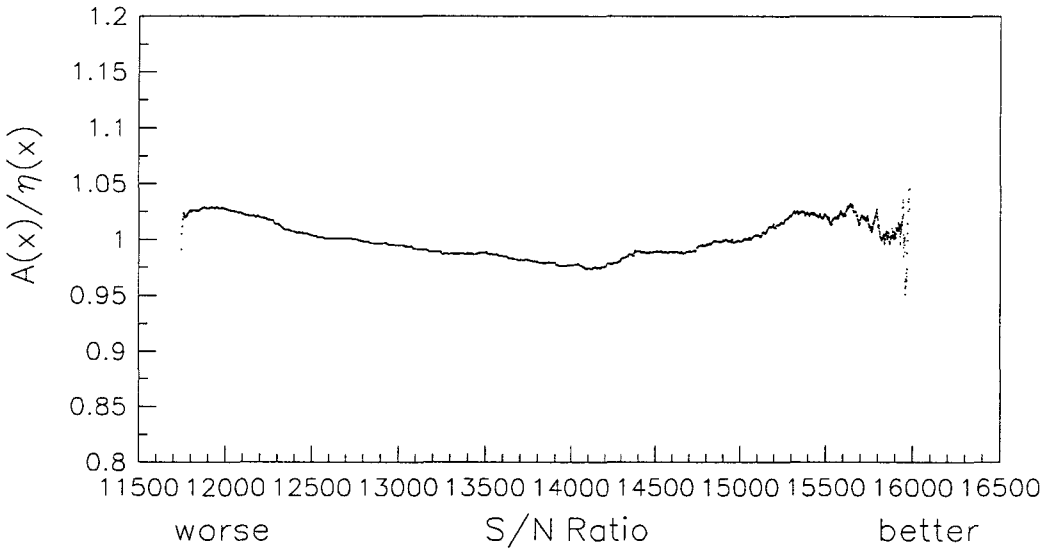

Figure 42: Ratio of $A(x)/\eta(x)$ as the function of the cut point. The ratio corresponds to the cross section of the ^{3}He(^{3}He,2p)^{4}He reaction. $\eta(x)$ and $A(x)$ is derived from the Eq.(20) and Eq.(21) stated in the text, respectively.

4 Discussion

4.1 Results

The cross sections for the ^{3}He(^{3}He,2p)^{4}He reaction were derived by the equation (19);

$$N = N_t \cdot N_b \cdot \sigma(E_{eff}) \cdot \int_L \eta(E) \cdot \epsilon(E)^{-1} \cdot dE,$$

where

N – number of counts for ^{3}He(^{3}He,2p)^{4}He reaction,
N_t – ^{3}He target density,
N_b – ^{3}He beam intensity,
E_{eff} – effective reaction energy,
$\eta(E)$ – the absolute detection efficiency,
$\epsilon(E)$ – stopping power.

In this work, the cross sections at the center-of-mass energy of E_{cm}=39.3, 41.3, 43.3 and 45.3 keV were obtained in June 2000. The results are presented in Fig. 43. Other experimental values such as the live time, the beam current, the target

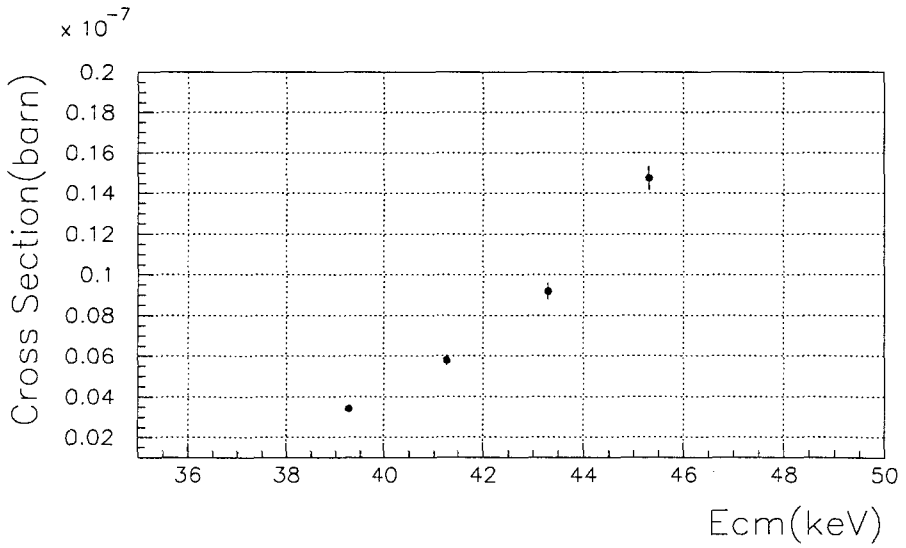

Figure 43: The observed cross sections for the ^{3}He(^{3}He,2p)^{4}He reaction are shown with statistical errors.

gas pressure, and the target gas temperature are shown in Table 6. The observed number of events for the ^{3}He(^{3}He,2p)^{4}He reaction and the background contribution from various sources are also shown in the same table.

Table 6: Experimental results of the measurement for the ^{3}He+^{3}He reaction.

E_{cm}(keV)	45.3	43.3	41.3	39.3
real time(sec)	94910	80404	80081	84944
live time(sec)	94857	80357	80034	84892
beam current(μA)	104	91.5	99.9	87.5
target press.(Torr)	7.51×10^{-2}	6.79×10^{-2}	6.79×10^{-2}	7.31×10^{-2}
target temp.(°C)	27.1	27.3	27.1	27.0
^{3}He+^{3}He(counts)	3344	1405	980	575
BG ^{3}He+d(counts)	2.6	0.9	0.9	0.7
BG other(counts)	4.0	3.4	3.4	3.6
cross section(barn)	1.48×10^{-8}	9.19×10^{-9}	5.79×10^{-9}	3.41×10^{-9}
s-factor(MeV·b)	5.18	5.22	5.47	5.62

The astrophysical S-factors were deduced from the equation (7);

$$\sigma(E) = \frac{S(E)}{E}\exp(-2\pi\eta) \ ,$$

where η is the Sommerfeld parameter and equal to in numerical unit;

$$2\pi\eta = 31.29 Z_1 Z_2 (\frac{\mu}{E})^{1/2} \ ,$$

where

Z_1 and Z_2 – nuclear charges of the interacting particles in the entrance channel,
μ – reduced mass (in units of amu),
E – center-of-mass energy (in units of keV).

The resulting $S(E)$ values from this work as well as previous data from Dwarakanath (1971) [39], Krauss (1987) [41] and LUNA (1998) [44] are shown in Fig. 44.

The obtained data are in a good agreement with the result of Krauss(1987), and they appear to be larger as the reaction energy is smaller. The accuracy of the data, both the statistical and the systematical one of the present measurement are better than those of the Krauss(1987). The statistical error of the present measurement at E_{cm}=45.3 keV is 1.7 %, which is better than that of Krauss(1987).

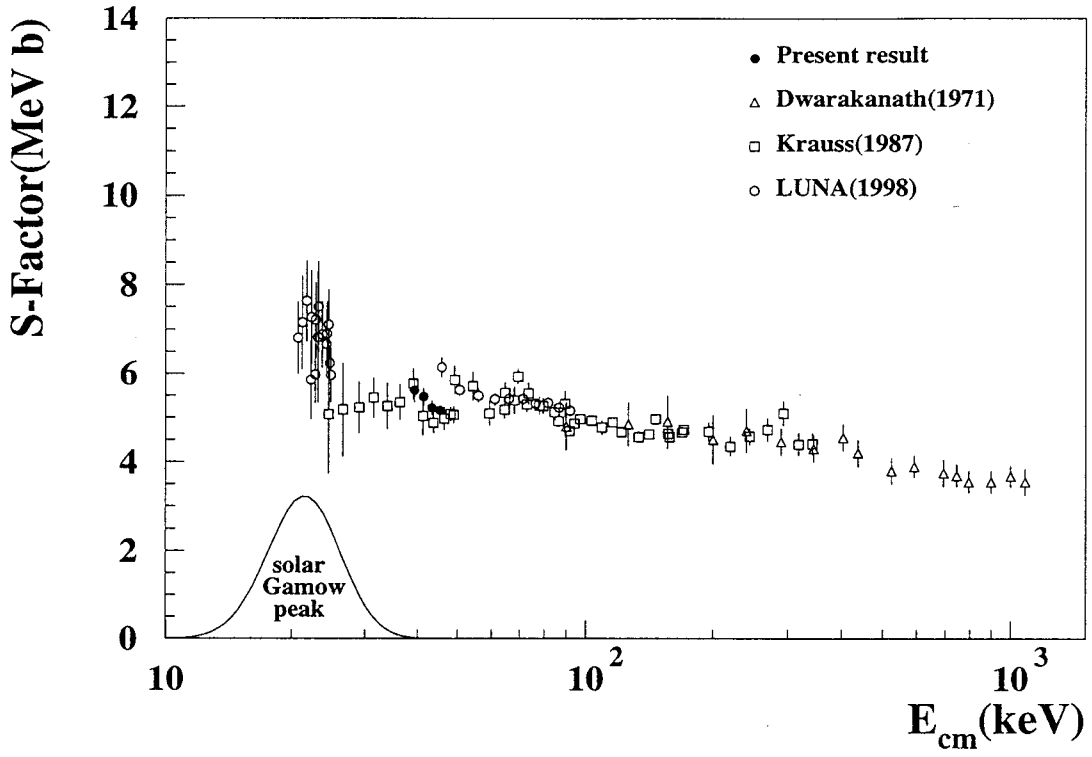

Figure 44: Astrophysical S-factor measured by the OCEAN experiment. The previous data are also plotted. The error bars show only statistical errors for all measurements.

As a result, the present experiment with OCEAN has proved to be more powerful compared to the other existing facilities, since it realized to deliver over 1 mA for $^3He^{1+}$ beam and 100 μA for $^3He^{2+}$ beam. Consequently, we can expect that the total event more than 100 counts in the center-of-mass energy range from 20 to 25 keV, could be obtained for a running time of about one month. Owing to OCEAN which provide not only singly charged but also doubly charged ^{3}He beam, one can continuously study wide region between 20 to 50 keV center of mass energy, which is not accessible for LUNA facility. It is important to investigate the enhancement for the ^{3}He(^{3}He,2p)^{4}He reaction due to the electron screening effects which will become manifest in the low energy region.

Comparison of systematical errors of this work with the other two results, Krauss and LUNA are shown in Table 7. The results encourage us to extend the measurements to the lower energy range.

Table 7: Systematic errors for present(OCEAN) and previous(Krauss(1987), LUNA(1998)) measurements.

	OCEAN	Krauss	LUNA
reaction energy(%)	0.15	0.27	0.09
beam intensity(%)	2	3	3
target density(%)	1.3	2	1
detection efficiency(%)	3	4	2

4.2 Future perspective

In the hydrogen burning proton-proton chain reaction, the only reaction that has so far been studied in the region of the Gamow peak energy is the ^{3}He(^{3}He,2p)^{4}He reaction. A more detailed study of this reaction at low energies is required to investigate the electron screening effect.

Having clarified applicability of our compact and bright accelerator facility OCEAN to the precise measurement for the ^{3}He(^{3}He,2p)^{4}He reaction at low energy, the measurement of the cross section at energies near the center of the Gamow peak is foreseen with a reasonable counting statics. The expected counting rate for the ^{3}He(^{3}He,2p)^{4}He reaction and the contribution of background events are shown in Fig. 45. In this estimation, the beam intensity of 1 mA for the $^3He^{1+}$ beam at $E_{cm} = 20 - 25$ keV, and of 100 μA for the $^3He^{2+}$ beam at $E_{cm} = 25 - 50$ keV,

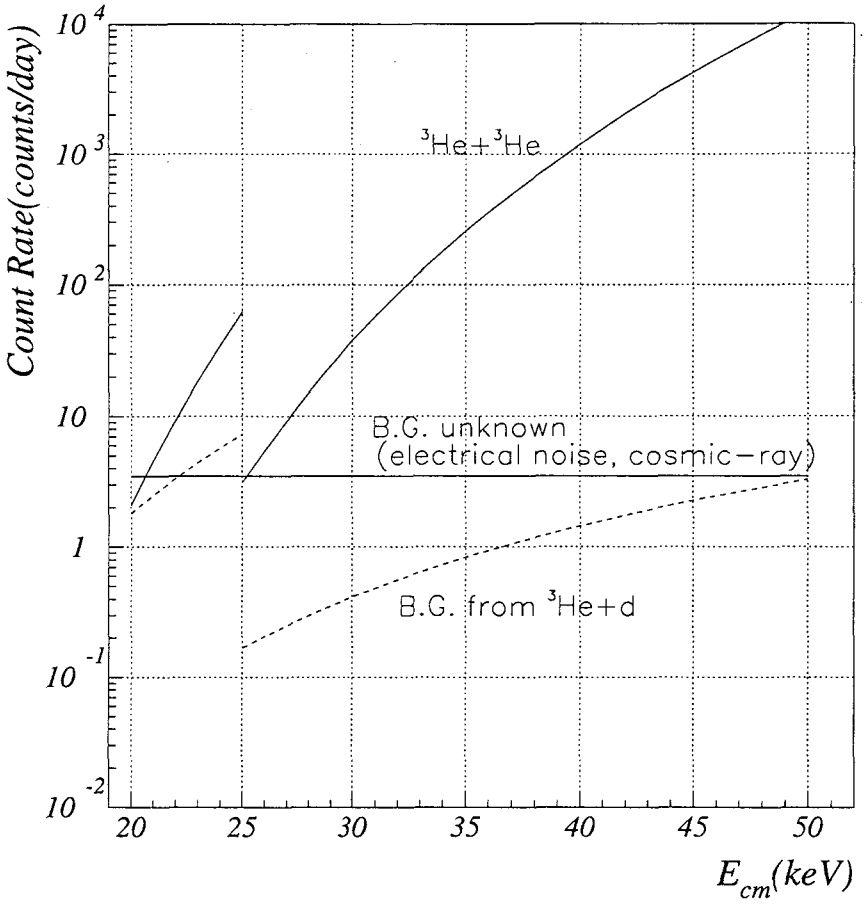

Figure 45: Expected counting rate for the ^{3}He(^{3}He,2p)^{4}He reaction and contribution of the background events. The beam intensity of 1 mA for the $^3He^{1+}$ beam at $E_{cm} = 20 - 25$ keV, and of 100 μA for the $^3He^{2+}$ beam at $E_{cm} = 25 - 50$ keV, and the target gas pressure of 0.1 Torr are assumed. Also, the S-factor of 5.4 MeV·b for the ^{3}He(^{3}He,2p)^{4}He reaction and 6.0 MeV·b for the d(^{3}He,p)^{4}He reaction are adopted. The deuteron contamination in the target gas and the contribution of the background caused by the electrical noise and cosmic rays measured in the present work are shown.

and the target gas pressure of 0.1 Torr are assumed. Also, the $S(0)$ values of 5.4 MeV·b for the ^{3}He(^{3}He,2p)^{4}He reaction and 6.0 MeV·b for the d(^{3}He,p)^{4}He reaction are assumed. For the background events, the deuterium contamination in the target gas of 0.2 ppm and the contribution of the background caused by the electrical noise and cosmic rays, are derived from the present measurements. In addition, the deuteron contamination in the $^3He^{1+}$ beam in the form of the HD^+ molecule of 1 ppm is assumed at $E_{cm} = 20 - 25$ keV. As it was mentioned above, a possibility appears to measure the cross section for the ^{3}He(^{3}He,2p)^{4}He reaction within the statistic error of about 10 % in the energy region of $E_{cm} > 21$ keV, at a running time only of about one month. It is estimated that the contribution of the background caused by electrical noise and cosmic rays, will be predominant rather than the one caused by the d(^{3}He,p)^{4}He reaction. In the reaction energy near 26 and 21 keV, the background contribution will be almost comparable to the ^{3}He(^{3}He,2p)^{4}He events. Therefore we must reduce the electrical noise and install the veto counter for the cosmic ray events.

5 Conclusion

1. The compact high-current and low energy ion accelerator facility OCEAN for the study of the thermonuclear ^{3}He(^{3}He,2p)^{4}He reaction, has been built and tested. It consist of ECR ion source NANOGAN^{TM}, a multi-electrode beam extraction system, a beam transport system including a dipole magnet and two quadrupole magnets, a windowless gas target system with a differential pumping system, a gas circulation and purification system, a beam calorimeter and ΔE-E counter telescope.

2. The OCEAN is more powerful facility compared to the other existing ones to study thermonuclear reactions, since it realized to deliver over 1 mA for $^3He^{1+}$ beam and 100 μA for $^3He^{2+}$ beam. Owing to singly and doubly charged beam, one can continuously study for the ^{3}He(^{3}He,2p)^{4}He reaction at wide region between 20 to 50 keV center-of-mass energy, which is not accessible for LUNA facility.

3. The astrophysical S-factors for the ^{3}He(^{3}He,2p)^{4}He reaction, derived from the cross section as $\sigma(E) = \frac{S(E)}{E}\exp(-2\pi\eta)$, were measured at four points of E_{cm}=39.3, 41.3, 43.3 and 45.3 keV respectively.

4. The resulting $S(E)$ values of 5.62, 5.47, 5.22 and 5.18 MeV·b for E_{cm}=39.3-45.3, respectively, are in agreement with the previous data of Krauss (1987) [41]. The statistical errors of the present data are reduced to one third of the previous data.

5. The systematic error for the reaction energy(0.15 %), beam intensity(2 %), target density(1.3 %) and detection efficiency(3 %) were evaluated respectively. The total systematic error of 3.8 % is as good as those of the previous data of LUNA(1998) [44].

6. It appears possible to study the ^{3}He(^{3}He,2p)^{4}He reaction in the solar Gamow energy region for running times of one month, with an improvement for background reduction.

6 Acknowledgments

The author gratefully acknowledges Professor T. Itahashi for valuable discussions and suggestions throughout this work, as well as for his kind encouragement. The author thanks Professor H. Ejiri, Y. Nagai, H. Toki, H. Ohsumi, Dr's K. Takahisa, N. Kudomi, K. Kume and S. Yoshida for their kind collaborations and discussions. He is also grateful to other members at RCNP and Department of Physics in Osaka University, Professor T. Kishimoto, A. Sakaguchi, Dr's S. Ajimura, I. Ogawa, Y. Shimizu, H. Kohri and T. Shima.

The present work was supported by Grant-in-Aid for Scientific Research from the Ministry of Education, Science, Culture and Sports of Japan.

Finally, the author wishes to thank his family, Kouichi and Atsuko Komori and Chie Hitsuishi for their supports and encouragements.

References

[1] J.N. Bahcall, Neutrino Astrophysics (Cambridge University, Cambridge, 1989)

[2] C. Rolfs and W.S. Rodney, Cauldrons in the Cosmos (University of Cicago Press, 1988)

[3] R. Davis, Jr., Prog. Part. Nucl. Phys. 32(1994)13.

[4] B.T. Cleveland, T. Daily, R. Davis, Jr., J.R. Distel, K. Lande, C.K. Lee, P.S. Wildenhain, and J. Ullman, Astrophys. J. 496(1998)505.

[5] Y. Fukuda *et al.* (Kamiocande Collaboration), Phys. Rev. Lett. 77(1996)1683.

[6] Y. Fukuda *et al.* (Super Kamiocande Collaboration), Phys. Rev. Lett. 82(1999)2430.

[7] P. Anselmann *et al.* (GALLEX Collaboration), Phys. Lett. B342(1995)440.

[8] J.N. Abdurashitov *et al.* (SAGE Collaboration), Phys. Lett. B328(1994)234.

[9] J.N. Bahcall, S. Basu and M.H. Pinsonneault, Phys. Lett. B433(1998)1.

[10] J.N. Bahcall, Phys. Lett. B338(1994)276.

[11] H.J. Assenbaum, K. Langanke and C. Rolfs, Z. Phys. A 327(1987)461.

[12] T.D. Shoppa, S.E. Koonin, K. Langanke and R. Seki, Phys. Rev. C48(1993)837.

[13] K. Langanke, T.D. Shoppa, C.A. Barnes, and C. Rolfs, Phys. Lett. B369(1996)211.

[14] J. Bang, L.S. Ferreira, E. Maglione and J.M. Hansteen, Phys. Rev. C53(1996)18.

[15] S. Engstler, G. Raimann, C. Angulo, U. Greife, C. Rolfs, U. Schröder, E. Somorjai, B. Kirch and K. Langanke, Phys. Lett. B279(1992)20.

[16] S. Engstler, G. Raimann, C. Angulo, U. Greife, C. Rolfs, U. Schröder, E. Somorjai, B. Kirch and K. Langanke, Z. Phys. A342(1992)471.

[17] T.D. Shoppa, M. Jeng, S.E. Koonin, K. Langanke and R. Seki, Nucl. Phys. A605(1996)387.

[18] Y. Boudouma, A.C. Chami and H. Beaumevieille, Nucl. Phys A617(1997)57.

[19] S. Engstler, A. Krauss, K. Neldner, C. Rolfs, U. Schröder and K. Langanke, Phys. Lett. B202(1988)179.

[20] P. Prati, C. Arpesella, F. Bartolucci, H.W. Becker, E. Bellotti, C. Broggini, P. Corvisiero, G. Fiorentini, A. Fubini, G. Gervino, F. Gorris, U. Greife, C. Gustavino, M. Junker, C. Rolfs, W.H. Schulte, H.P. Trautvetter and D. Zahnow, Z. Phys. A350(1994)171.

[21] H. Andersen, J.F. Ziegler, The Stopping and Range of Ions in Matter (Pergamon, New York, 1977).

[22] R. Golser and D. Semrad, Phys. Rev. Lett. B66(1991)1831.

[23] H. Costantini, A. Formicola, M. Junker, R. Bonetti, C. Broggini, L. campajola, P. Corvisiero, A. D'Onofrio, A. Fubini, G. Gervino, L. Gialanella, U. Greife, A. Guglielmetti, C. Gustavino, G. Imbriani, A. Ordine, P.G. Prada Morini, P. Prati, V. Rogalla, C. Rolfs, M. Romano, F. Schümann, O. Straniero, F. Strieder, F. Terrasi, H.P. Trautvetter and S. Zavatarelli, Phys. Lett. B482(2000)43.

[24] E.G. Adelberger, S.M. Austin, J.N. Bahcall, A.B. Balantekin, G. Bogaert, L.S. Brown, L. Buchmann, F.E. Cecil, A.E. Champagne, L. de Braeckeleer, C.A. Duba, S.R. Elliott, S.J. Freedman, M. Gai, G. Goldring, C.R. Gould, A. Gruzinov, W.C. Haxton, K.M. Heeger, E. Henley, C.W. Johnson, M. Kamionkowski, R.W. Kavanagh, S.E. Koonin, K. Kubodera, K. Langanke, T. Motobayashi, V. Pandharipande, P. Parker, R.G.H. Robertson, C. Rolfs, R.F. Sawyer, N. Shaviv, T.D. Shoppa, K.A. Snover, E. Swanson, R.E. Tribble, S. Turck-Chièze and J.F. Wilkerson, Rev. Mod. Phys. 70(1998)1265.

[25] V.N. Feticov and Yu.S. Kopysov, Phys. Lett. B40(1972)602.

[26] W.A. Fowler, Nature 238(1972)24.

[27] J.N. Barcall and R. Davis, Jr., Science 191(1976)264.

[28] V.N. Feticov and Yu.S. Kopysov, Nucl. Phys. A239(1975)511.

[29] V. Castellani, S. Degl'Innocenti and G. Fiorentini, Astron. Astrophys. 271(1993)601.

[30] H.B. Mak, E.M. Mann and R.W. Kavanagh, Bull. Am. Phys. Soc. 17(1972)1180.

[31] M.L. Halbert, D.C. Hensley and H.G. Bingham, Phys. Rev. C8(1973)1226.

[32] C. Wong, R.C. Haight, S.M. Grimes, J.D. Anderson, J.C. Davis, J.W. McClure and B.A. Pohl, Bull. Am. Phys. Soc. 18(1973)652.

[33] L.S. Cardman, B.P. Fivozinsky, J.S. O'Connell and S. Penner, Bull. Am. Phys. Soc. 18(1973)78.

[34] L.W. Fagg, W.L. Bendel, N. Ensslin and E.C. Jones, Jr., Phys. Lett. B 44(1973)163.

[35] W. Viefers, W. von Witsch and A. Richter, Nucl. Phys. A 248(1975)518.

[36] A.B. McDonald, T.K. Alexander and J.R. Beene, Nucl. Phys. A 288(1977)529.

[37] A.D. Bacher and T.A. Tombrello, Rev. Mod. Phys. 37(1965)433.

[38] N.M. Wang, V.N. Novatskiĭ, G.M. Osetinskiĭ, N.K. Chien, and I.A. Chepepurchenko, Nucl. Phys. 3(1966)777.

[39] M.R. Dwarakanath and H. Winkler, Phys. Rev. C 4(1971)1532.

[40] M.R. Dwarakanath, Phys. Rev. C 9(1971)805.

[41] A. Krauss, H.W. Becker, H.P. Trautvetter, C. Rolfs and K. Brand, Nucl. Phys. A 467(1987)273.

[42] U. Greife, C. Arpesella, C.A. Barnes, F. Bartolucci, E. Bellotti, C. Broggini, P. Corvisiero, G. Fiorentini, A. Fubini, G. Gervino, F. Gorris, C. Gustavino, M. Junker, R.W. Kavanagh, A. Lanza, G. Mwzzorani, P. Prati, P. Quarati, W.S. Rodney, C. Rolfs, W.H. Schulte, H.P. Trautvetter and D. Zahnow, Nucl. Instr. and Meth. A 350(1994)327.

[43] C. Arpesella, E. Bellotti, C. Broggini, P. Corvisiero, G. Fiorentini, A. Fubini, U. Greife, C. Gustavino, M. Junker, J. Lambert, P. Prati, W.S. Rodney, C. Rolfs, H.P. Trautvetter, D. Zahnow and S. Zavatarelli, Phys. Lett. B 389(1996)452.

[44] M. Junker, *et al.* (LUNA Collaboration), Phys. Rev. C 57(1998)2700.

[45] R. Bonetti, *et al.* (LUNA Collaboration), Phys. Rev. Lett. 82(1999)5205.

[46] A.J.T. Holmes, Phys. Rev. A19(1979)389.

[47] R.E. Brown and N. Jarmie, Phys. Rev. C41(1990)1391.

[48] T. Itahashi, K. Takahisa, N. Kudomi, T. Iki, S. Yoshida, H. Toki, H. Ejiri, H. Ohsumi and M. Komori, Rev. Sci. Instr. 69(1998)1032.

[49] T. Itahashi, N. Kudomi, K. Kume, K. Takahisa, S. Yoshida, H. Ejiri, H. Toki, Y.ZNagai, H. Ohsumi, M. Komori and K. Yamasaki Rev. Sci. Instr. 71(2000)1075.

[50] NANOGAN instruction book

[51] P. Sortais, C. Bieth, P. Foury, N. Lecesne, R. Leroy, J. Mandin, C. Marry, J.Y. Pacquet, E. Robert and A.C.C. Villari, *Proc. of the 12th Intern. Workshop on ECR ion sources*, RIKEN, Japan (1995) p. 45.

[52] T. Itahashi, K. Takahisa, N. Kudomi, T. Iki, S. Yoshida, H. Toki, H. Ejiri, H. Ohsumi and M. Komori, *Proc. of the 11th Symposium on Accel. Sci. and Tech.,* Harima, Japan, (1997) p. 151.

[53] R. Lery, J.C. Angelique, P. Bertand, G.B. Blank, M. Ducourtieux, P. Foury, N. Lecesne, A. Lepine, M. Lewitowicz, C.F. Liang, J. Mandin, C. Marry, L. Maunoury, J. Mercier, J. Obert, N.A. Orr, J.Y. Pacquet, P. Paris, J.C.Potier, J.C. Putaux, E. Robert, M.G. Saint-Laurent, P. Sortais and A.C.C. Villari, *Proc. of the 12th Intern. Workshop on ECR ion sources*, RIKEN, Japan (1995) p. 57.

[54] S. Fu, A. Kitagawa and S. Yamada, *NIRS Report*, National Institute of Radiological Science, Anagawa Chiba 263 Japan (unpublished)

[55] T. Itahashi, K. Takahisa, N. Kudomi, T. Iki, S. Yoshida, H. Toki, H. Ejiri, H. Ohsumi and M. Komori, *RCNP Annual Report*, RCNP(1997) p. 77.

[56] T. Iki, Ph M Thesis, Osaka Univ. (1998)

[57] H. Wollnik, B. Hartmann and M. Berz, AIP Conference Proceedings 177(1988)74

[58] G.S. Chulick, Y.E. Kim, R.A. Rice, Nucl. Phys. A551(1993)255.

[59] Y. Saitoh, *Workshop of high brightness ion source for nuclear astrophysics*, RCNP, Japan (1996) (unpublished)

[60] J.F. Ziegler, Program SRIM-2000, IBM Research, http://www.research.ibm.com/ionbeams/SRIM/SRIMINTR.HTM.

[61] J.F. Ziegler, J.P. Biersack nad U. Littmark, The Stopping and Range of Ions in Solids (Pergamon, Oxford, 1985).

[62] R. Golser and D. Semrad, Nucl. Instr. and Meth. B69(1992)18.

[63] T. Itahashi, H. Ohsumi, K. Takahisa, N. Kudomi, M. Komori, T. Iki, H. Toki and H. Ejiri, *RCNP Annual Report*, RCNP(1996) p. 148.